Combined Effects of Surfactant and Viscoelasticity on Drop Dynamics

by

Mohammad Nabizadehmashhadtoroghi

A Dissertation Submitted to the
Graduate School of Sciences and Engineering
in Partial Fulfillment of the Requirements for
the Degree of

Master of Science

in

Mechanical Engineering

August 27, 2018

Combined Effects of Surfactant and Viscoelasticity on Drop Dynamics

Koç University

Graduate School of Sciences and Engineering

This is to certify that I have examined this copy of a master's thesis by

Mohammad Nabizadehmashhadtoroghi

and have found that it is complete and satisfactory in all respects,
and that any and all revisions required by the final
examining committee have been made.

Committee Members:

_____

Prof. Dr. Metin Muradoğlu

_____

Prof. Dr. Burak Erman

_____

Assoc. Prof. Ayşe Gül Güngör

Date: _____

ABSTRACT

Combined effects of surfactant and viscoelasticity on droplet dynamics are studied in an axisymmetric tube using a front-tracking method. Both rising and sedimenting droplet cases are considered. Viscoelasticity is contained in the droplet fluid while surfactant is contained in the continuous phase. The FENE-CR model is used to account for droplet liquid viscoelasticity. The incompressible Navier-Stokes equations are solved fully coupled with the surfactant evolution and the viscoelastic model equations in the entire computational domain. The surface tension is related to the interfacial surfactant concentration by a non-linear equation of state. Extensive simulations are performed to investigate the effects of both viscoelasticity and surfactant on droplet dynamics in nearly spherical, dimpled ellipsoidal cap and skirted regimes. It is found that the surfactant-induced Marangoni stresses generally counteract the viscous shear stresses to reduce mobility of the interface and thus decrease the terminal velocity of the droplet. This effect is most pronounced in the nearly spherical regime in which the interface is almost fully immobilized making the droplet behave like a solid sphere. In the dimpled ellipsoidal cap and skirted regimes, the effects of surfactant diminish significantly since the surfactant adsorbed at the leading edge is quickly convected toward the rear edge rendering the most part of the interface clean. The viscoelastic stresses are found to be nearly uniform in the nearly spherical regime and thus have negligible influence on drop dynamics. However, the viscoelastic stresses concentrate around the rear stagnation point and induce an indentation there especially in the dimpled ellipsoidal cap and skirted regimes. This effect is significantly amplified in the presence of the surfactant leading to creation of a hole at the drop centerline in extreme cases.

ÖZETÇE

Çözülebilir yüzey aktif maddesi ve viskoelastisitenin damlacık dinamiği üzerindeki etkileri arayüz-izleme yöntemi kullanılarak sayısal olarak incelendi. Hem yükselen hem de çöken damlacık durumları göz önünde bulunduruldu. Bu çalışmada, viskoelastisite damlacık akışkanına eklenirken çözülebilir yüzey aktif maddesi ise dıştaki akışkana ilave edildi. Damlacık akışkanındaki viskoelastik etkiler FENE-CR modeli kullanılarak hesaba katıldı. Sıkıştırılamaz Navier-Stokes denklemleri yüzey aktif maddesi evolüsyon denklemleri ve viskoelastik model denklemleriyle birlikte tam bağlı olarak (fully-coupled) bütün hesaplama bölgesinde sayısal olarak çözüldü. Yüzey gerilmesi doğrusal olmayan bir durum denklemi kullanılarak ara-yüzeydeki yüzey aktif maddesi konsantrasyonuna bağlandı.

Yüzey aktif maddesi ve viskoelastisitenin kombine etkilerini incelemek amacıyla neredeyse-küresel, çökmeli elipsoit kep ve etekli damlacık rejimleri için çok sayıda sayısal simülasyon yapıldı. Yüzey aktif maddesinden kaynaklanan Marangoni gerilmesinin genel olarak viskoz kayma gerilmesinin aksi yönde etki ettiği, ara-yüzeyin hareketliliğini kısıtladığı ve bunun sonucu olarak damlacığın hızını azalttığı bulundu. Bu etkinin en çok neredeyse-küresel damlacık durumunda belirgin olduğu tespit edildi. çökmeli elipsoit kep ve etekli damlacık rejimlerinde ise damlacığın ön kısmından adsorbe edilen yüzey aktif maddesinin hızlı bir şekilde damlacığın arkasına doğru konvetke olması nedeniyle ara-yüzeyin büyük kısmının temiz kaldığı ve dolayısıyla yüzey aktif maddesinin etkilerinin büyük oranda azaldığı gözlendi. Neredeyse-küresel rejimde damlacık içindeki viskoelastik gerilme dağılımının üniform olduğu ve dolayısıyla damlacık dinamiğine etkisinin ihmal edilebilir mertebede kaldığı tespit edildi. Çökmeli elipsoit kep ve etekli damlacık rejimlerinde ise viskoelastik gerilmelerin damlacığın arkasındaki durma noktası civarında yoğunlaştığı ve damlacığın arkasında çökme oluşmasına neden olduğu gözlendi. Bu etkinin yüzey aktif maddesi eklenmesiyle daha da kuvvetlendiği ve ekstrem durumlarda arkadaki çökmenin içeri doğru ilerleyerek damlacık ortasında delik oluşmasına yok açtığı bulundu.

ACKNOWLEDGMENTS

This work is supported by the scientific and Technical Research Council of Turkey (TUBITAK), Grant No. 115M688.

TABLE OF CONTENTS

LIST OF TABLES

LIST OF FIGURES

NOMENCLATURE

$\mathbf{u}$	velocity vector
p	pressure
ρ_i	density of the droplet
ρ_o	density of the ambient fluid
$\mu_{s,i}$	solvent viscosity of the droplet
$\mu_{s,o}$	solvent viscosity of the ambient fluid
$\mu_{p,i}$	polymeric viscosity of the droplet
$\mu_{p,o}$	polymeric viscosity of the ambient fluid
λ_i	relaxation time of the droplet
λ_o	relaxation time of the ambient fluid
t	physical time
t^*	time scale
s	arc length
σ	surface tension coefficient
κ	curvature
x	the point at which the body force of momentum equations is evaluated
x_f	a point at the interface
I	Indicator function
M_s	total mass of surfactant
A	surface area of interface
δ	Dirac delta function
a	droplet radius
R	channel radius

L	channel Length
Γ	surfactant concentration at the interface
Γ_{eq}	surfactant concentration value at the equilibrium state
Γ_{∞}	maximum surfactant concentration at the interface
D_s	diffusion coefficient at the interface
D_c	diffusion coefficient in the bulk
D_{co}	molecular diffusion coefficient
C	C bulk surfactant concentration
C_{∞}	maximum bulk surfactant concentration
C_s	surfactant concentration in fluid immediately adjacent to the interface
σ_s	surface tension coefficient of a clean interface
$\mathcal{L}$	length scale
$\mathcal{U}$	velocity scale
Re	Reynolds number
Ca	Capillary number
Pe_s	Peclet number based on interface surfactant diffusivity
Pe_c	Peclet number based on bulk surfactant diffusivity
Da	Damkohler number
Bi	Biot number
Wi	Weissenberg number
α	solvent viscosity ratio
k_a	adsorption coefficient
k_b	desorption coefficient
β	elasticity number
$\mathbf{E}$	extra stress or conformation tensor
$\boldsymbol{\tau}$	extra stress tensor
F	stretch function

Chapter 1

INTRODUCTION

Multiphase flows are ubiquitous in a wide range of natural processes, biological systems and industrial applications. Many of our daily activities are also directly or indirectly related to multiphase flows. Common examples include the human respiratory system [Grotberg, 2011], breaking waves, oil production and process industry [Larson et al., 1981, Olbricht, 1996], spray combustion devices, fluidized beds and bubbly flows [Clift et al., 2005]. Both physical modeling and numerical computation of multiphase flows are notoriously difficult mainly due to the sharp interface separating two fluids. The interface evolves in time and undergoes large deformations often leading to topological changes. Numerical difficulties arise from tracking the interface both in time and space, and resolving discontinuous variations of material properties across the evolving interface during the course of computation [Tryggvason et al., 2011].

Multi-physics effects such as viscoelasticity and soluble surfactant add further complexity into the problem. Surfactants are present in fluids either as contaminants that are difficult to remove or are added to liquids to manipulate multiphase flow systems. Surfactant molecules tend to collect at the fluid-fluid interface, create a buffer zone between two immiscible fluids, interact with the cohesive forces between the fluid molecules and thus reduce the surface tension [Levich, 1992]. A non-uniform distribution of interfacial surfactant concentration results in Marangoni stresses which critically influence dynamics of multiphase flows. The striking example is the retardation of contaminated buoyant bubble rising in a quiescent liquid. It has been shown by numerous experimental and computational studies that a small bubble behaves like a solid sphere in the presence of surfactant and its terminal velocity approach that of a solid sphere in the limit of a nearly spherical regime in which bubble deformation is negligibly small. This interesting behavior was

first explained by Frumkin and Levich [Frumkin, 1947] who pointed out that the surfactant molecules adsorbed at the interface are convected toward the trailing edge causing large Marangoni stresses that oppose to flow and act to immobilize the interface. Surfactants particularly play a critical role in pulmonary flows [Grotberg, 2001, Grotberg, 2011] . Pulmonary surfactant is absorbed on the liquid-lining that covers surface of airways and alveoli and reduces the surface tension on the liquid-gas interface, which reduces the work required to expand the lung at each breath. Pulmonary surfactant also regulates the inflation and deflation of alveoli, and make them act in unison. Deficiency of surfactant results in respiratory distress syndrome (RDS) [Manual, 2004] while excess of it may prevent re-opening of airways [Grotberg, 2001]. Surfactants are also widely used in a variety of industrial and biomedical applications [Sjoblom, 2005].

Viscoelastic fluids usually contain long-chain molecules such as polymers and proteins, and exhibit a non-linear relationship between shear stress and the rate of strain in contrast with the Newtonian fluids in which shear stress is linearly related to the rate of strain. In addition, viscoelastic fluids also exhibit the memory effects, i.e., they behave both as a viscous and an elastic medium. An important feature of the viscoelastic fluids is that they have non-zero normal stress differences caused by the interaction of polymer molecules with the flow, i.e., the polymer molecules contained in a viscoelastic liquid stretch along the streamlines and exert non-isotropic stresses on the fluid to induce non-zero normal stress differences. Note that the normal stress differences are identically zero in Newtonian fluids. Due to these normal stress differences, viscoelastic liquids show various exotic behaviors such as reversal of direction in the secondary flow in a stirred beaker [Hill, 1972], the Weissenberg or rod climbing effect [Garner and Nissan, 1946], die swell effect [Tanner, 1970] and turbulence at low Reynolds number [Groisman and Steinberg, 2000]. These striking features of viscoelastic liquids have been widely exploited to perform useful functions especially in microfluidic applications. For instance, microfluidic memory and control device [Beris and Housiadas, 2010], microfluidic rectifier [Bertola, 2009], nonlinear viscoelastic flow resistor [Beris and Housiadas, 2010], synthesis of non-spherical particles [Bertola, 2013] and enhanced mixing in microchannels [Bertola and Wang, 2015]. In addition, most biological fluids contain proteins and thus exhibit viscoelastic behavior. For this reason, the biological cells are often modeled as viscoelastic liquids [Tasoglu et al., 2010].

The surfactant molecules are typically long-chain molecules composed of hydrophilic heads and hydrophobic tails, and usually bring viscoelasticity into the host fluid [Tretheway and Leal, 1999]. In addition, surfactants are added deliberately to manipulate viscoelastic multi-phase flows systems. Therefore it is of fundamental importance to understand the combined effects of surfactant and viscoelasticity on interfacial flows. Highly non-linear and strong interactions between viscoelasticity and fluid-fluid interface result in very rich dynamics and thus make computational simulations a challenging problem for computational fluid dynamics. In the common viscoelastic models such as the Oldroyd-B and the finitely extensible nonlinear elastic (FENE) models, the polymer molecules are assumed to be dumbbells having two beads connected by a massless spring. In spite of the simplicity of the dumbbell models, the resulting set of partial differential equations are highly non-linear and become extremely stiff due to the large disparity in time scales especially at a high Weissenberg number which is a non-dimensional measure of the fluid elasticity [Chen et al., 2013, Marchal and Crochet, 1987]. This is known as the high Weissenberg number problem (HWNP). The viscoelastic model equations must be solved fully coupled with the flow equations to resolve strong interactions between viscoelasticity, fluid flow and interface [Owens and Phillips, 2002]. The conventional numerical methods break down and become unstable at high Weissenberg numbers mainly due to the failure to properly approximate the exponential growth of viscoelastic stresses in regions of high shear rates. The existence of an evolving interface and jumps in material properties makes the problem even more complicated and challenging in multi-phase flow systems [Sarkar and Schowalter, 2000]. Izbassarov and Muradoglu [Izbassarov and Muradoglu, 2015, Izbassarov and Muradoglu, 2016] have recently developed a highly efficient and robust finite-difference/front-tracking method for particle-resolved simulations of interfacial viscoelastic flows in a wide range of Weissenberg numbers, i.e., $0 \leq Wi \leq 100$. In this method, the convective terms in viscoelastic constitutive equations are approximated using a fifth-order upwinded WENO-Z scheme [Borges et al., 2008] while the log-conformation method [Fattal and Kupferman, 2005] is employed to overcome high Weissenberg number problem. The method can accommodate virtually any viscoelastic model belonging to the Oldroyd-B and FENE families. We essentially use this method to account for the viscoelasticity in the present study.

Numerical simulation of soluble surfactant also poses a challenging problem mainly due

to difficulty of handling mass exchange between the bulk fluid and interface. Bulk and interfacial surfactant concentrations evolve by their convection-diffusion equations that must be solved fully coupled with the viscoelastic flow equations. Muradoglu et al. [Muradoglu and Tryggvason, 2008 Muradoglu and Tryggvason, 2014] have developed a front-tracking method to simulate the effects of surfactant on multiphase flows. In this method, the bulk surfactant concentration is allowed to vary both in space and time according to a convection-diffusion equation and both the bulk and interface surfactant concentration equations are solved coupled with the incompressible flow equations. The surfactant mass transfer between the bulk fluid and the interface is achieved in a conservative manner by distributing the amount of surfactant adsorbed by the interface as a negative source term for the bulk concentration equation near the interface using the Peskin's cosine distribution [Peskin, 1977].

In the present study, soluble surfactant is included into the finite-difference/front-tracking viscoelastic multiphase flow solver to study the combined effects of viscoelasticity and surfactant on dynamics of a gravity-driven droplet in a circular tube. Both rising and sedimenting droplet cases are considered. Viscoelasticity is contained in the droplet fluid while surfactant is contained in the continuous phase. The FENE-CR model is used to account for droplet liquid viscoelasticity. The incompressible Navier-Stokes equations are solved fully coupled with the surfactant evolution and the viscoelastic model equations in the entire computational domain. The surface tension is related to the interfacial surfactant concentration by a non-linear equation of state.

Drop dynamics in confined geometries has been a subject of many experimental, theoretical and numerical studies due to its relevance in a wide range of engineering applications [Olbricht, 1996]. The effects of surfactant were first studied for the simple case of spherical bubbles. Bel Fdliha and Duineveld [Bel Fdhila and Duineveld, 1996] and more recently Zhang and Finch [Zhang and Finch, 2001] experimentally investigated the effects of surfactant on nearly spherical bubbles/droplets in unconfined conditions. Bel Fdliha and Duineveld [Bel Fdhila and Duineveld, 1996] examined dependence of steady terminal rise velocity of bubble on the bulk surfactant concentration while Zhang and Finch [Zhang and Finch, 2001] studied the effects of bulk surfactant concentration on the transient motion of a spherical bubble for three different bulk surfactant concentrations. They both found that bulk surfactant concentration influences the distance to reach a steady-state significantly but the

steady rise velocity is insensitive to the bulk surfactant concentration. Borhan and Pallinti [Borhan and Pallinti, 1995, Borhan and Pallinti, 1999] performed a detailed experimental study to investigate motion, deformation and breakup of clean gas bubbles through capillaries. Later Almatroushi and Borhan [Almatroushi and Borhan, 2004] examined the effects of surfactant on bubble dynamics with significant deformations and found that the surfactant reduces terminal velocity of small bubbles while it enhances the mobility of large bubbles due to increased liquid film thickness between the bubbles and the tube wall. Zhang et al. [Zhang and Finch, 2001] experimentally studied the effect of the surfactant on the terminal velocity of a rising bubble. They observed the retardation effect of surfactant on the motion of droplet and the fact that the steady-state velocity is independent of the concentration in a wide range. On the theoretical and computational side, Stone and Leal [Stone and Leal, 1990] performed simulations to investigate the deformation and breakup of a droplet in extensional creeping flows under the effect of insoluble surfactant at low Reynolds numbers using a boundary-integral method with the time-dependent convective-diffusion equation of surfactant evolution. He et al. [He et al., 1991a] studied the retardation effect of surfactant adsorption on a fluid sphere interface for an axisymmetric creeping flow in the limit of sorption-controlled regime. They found that the surfactant-induced Marangoni stresses generally retard the fluid particle velocity in otherwise quiescent bulk fluid while the surfactant-induced Marangoni stresses can increase the velocity of the fluid particle in a Poiseuille flow when the particle velocity is small compared to the Poiseuille centreline velocity. He et al. [He et al., 1991b] examined effects surfactant on a spherical fluid droplet in a stagnant cap regime in which strong convection clears the front part of the droplet making the interfacial surfactant confined on the back with a sharp transition. They obtained an exact solution for the terminal velocity, at low Reynolds numbers, in terms of the cap angle when a linear equation of state is used. Takemura and Yabe [Takemura and Yabe, 1999] experimentally and numerically investigated the effect of contamination on a carbon-dioxide bubble rising in a large quiescent water bath. They showed the retardation effect of surfactant on a buoyancy-driven bubble, where the bubble behaves more like a solid sphere than a fluid sphere (also shown by Clift et al. [Clift et al., 2005]). They also observed the immobilization effect of surfactant in this case. Later, Eggleton and Stebe [Eggleton and Stebe, 1998] numerically studied the effects of surfactant on a de-

formable droplet in an extensional flow to investigated how surfactant concentration changes the hydrodynamics of the droplet and affects the deformability of the droplet. They considered both insoluble and soluble surfactant cases. Their main finding is that contaminated droplets deform more in the absence of surfactants at a given capillary number (Ca) and breakup at lower Ca and stagnant caps form at the drop tips when stable drop shapes are attained in the insoluble limit while surfactant solubility eliminates these caps and diminishes the deformation. Johnson and Borhan [Johnson and Borhan, 1999] performed boundary integral simulations to examine the effect of insoluble surfactant on an axisymmetric pressure driven droplet in a tube under low Reynolds numbers. They found that the drop mobility increases as surface coverage increases, attaining maximum mobility at about 50% of initial coverage for surfactants with strong cohesive interactions. They also observed flow patterns corresponding to uniform retardation of interface mobility as a fully immobilized interface is approached with increasing surface convection and the formation of a stagnant cap at the trailing end of the drop in the surface-convection-dominated regime. James and Lowengrub [James and Lowengrub, 2004] studied an axisymmetric numerical method for the simulation of insoluble surfactant on interfacial flow using a volume-of-fluid (VOF) method. A non-linear convection-diffusion equation is used to model the surfactant evolution. They observed that surfactant accumulates at the droplet tips and causes significant Marangoni effects. Almatroushi and Borhan [Almatroushi and Borhan, 2004] experimentally studied the effect of surfactant on the Buoyancy-driven motion of bubbles and drops in a vertical tube. They observed the retardation effect of surfactant on a viscous droplet and also showed that surfactant has weaker effect on the surfactant-retarded bubble. Lee and Pozrikidis [Lee and Pozrikidis, 2006] implemented a numerical method by combining the Peskin's immersed-interface formulation, the diffuse-interface approximation, a variant of the Chorin's projection method and a finite-volume method for the convection-diffusion equation of surfactant evolution on the interface. They used an integral identity to smooth the physical properties of the fluids. They found that surfactant can cause immobility of the droplet. More recently, Takagi and Matsumoto [Takagi and Matsumoto, 2011] performed experiments on the effect of surfactant on a bubbly flow in water and showed that surfactant can dramatically change the behavior of the bubble and specially, the reduction of terminal velocity in the contaminated environment was observed. Full Navier-Stokes

simulations have been more recently performed using various approaches. Sugiyama et al. [Sugiyama et al., 2001] solved the full Navier-Stokes with finite-rate mass exchange between the interface and bulk fluid in a similar fashion as done by Cuento et al. [Cuenot et al., 1997] but allowing bubble deformations. They managed to perform computations with significant bubble deformations but they ignored the wall effects and also imposed a terminal velocity, which is not easy to achieve experimentally. To overcome these difficulties, Muradoglu and Tryggvason [Muradoglu and Tryggvason, 2008] developed a front-tracking method to investigate the effect of surfactant on interfacial flows for the general case of fully deformable interfaces with virtually any boundary conditions including solid walls. They later extended their method to simulate the effects of soluble surfactant in fully 3D multiphase flow [Muradoglu and Tryggvason, 2014]. Tasoglu et al. [Tasoglu et al., 2008] also used front-tracking method to study the effect of soluble surfactant on the unsteady motion and deformation of buoyancy driven droplet in a confined axisymmetric tube using front-tracking method. Front-tracking method was also used by Olgac and Muradoglu [Olgac and Muradoglu, 2013], they computationally investigated the effects of soluble and insoluble surfactant in the Bretherton problem. They showed how the surface tension shows different levels of sensitivity when the elasticity number changes.

Effects of viscoelasticity on bubbles/drops in small capillaries have been subject of a few studies. Early experimental studies [Hassager, 1979, Liu et al., 1995] revealed that an asymmetric knife-like cusp may develop at a trailing edge of a buoyantly rising bubble in a viscoelastic fluid under certain conditions. They also found that the formation of such a cusped tail is also accompanied by a jump discontinuity of rising when the bubble size exceeds a critical value. Later, Herrera-Velarde et al. [Herrera-Velarde et al., 2003] performed a particle image velocimetry experimental study and demonstrated the existence of negative wake downstream of the bubble for a volume just above the critical value. They found that the wall confinement does not change the critical volume at which the velocity jump occurred. Sostarecz and Belmonte [Sostarecz and Belmonte, 2003] experimentally studied motion and deformation of a viscoelastic drop falling through a viscous Newtonian fluid and revealed that steady shapes exhibiting a dimple at the trailing edge of the droplet. They showed that the dimple extends further into the drop and causes instability as the drop size is increased. A few computational studies have been also performed to examine

the effects of viscoelasticity on drop/bubble dynamics in confined geometries. Noh et al. [Noh et al., 1993] used the finitely extensible nonlinear elastic-Chilcott-Rallison FENE-CR model [Chilcott and Rallison, 1988] to simulate buoyant bubbles rising in dilute polymer solutions and showed the tendency of transition from a prolate shape to a cusped shape as the capillary number increases. Malaga and Rallison [Malaga and Rallison, 2007] performed boundary integral method simulations to examine the axisymmetric bubble deformation in a FENE-CR model fluid. They pointed out a small stretch at the rear stagnation point qualitatively resembling the bubble deformation in a dilute polymer solution observed in the experiment. However, they did not find any evidence of a jump discontinuity in the bubble rising speed. Hooper et al. [Hooper et al., 2001] performed finite element simulations using the Oldroyd-B model to investigate the deformation of a viscoelastic drop suspended in another viscoelastic fluid in a creeping flow regime. They found that fluid viscoelasticity causes transient drop extension and retraction phenomena. You et al. [You et al., 2008] performed extensive boundary element simulations to investigate the confined motion of a drop in a cylindrical tube is investigated for the case in which one of the two phases is viscoelastic. They found that a Newtonian drop develops an extending trailing edge when it is immersed in a viscoelastic fluid, while a viscoelastic drop in a Newtonian fluid experiences an indentation around the rear stagnation point. They also reported that, under certain conditions, a cusped drop appears due to fluid viscoelasticity that triggers shape instability. Recently, Izbassarov and Muradoglu [Izbassarov and Muradoglu, 2015] developed a finite-difference/front-tracking method for computational modeling of viscoelastic two-phase systems and performed simulations for various gravity-driven two-phase viscoelastic flow systems in confined geometries but their main purpose was to validate the new code. They later used the finite-difference/front-tracking method to study the effects of viscoelasticity on the droplet when it impacts a solid interface [Izbassarov and Muradoglu, 2016] and the effects of viscoelasticity on the droplet formation and breakup dynamics in a flow focusing configuration [Nooranidoost et al., 2016].

As pointed out earlier, both viscoelasticity and surfactant coexist in many two phase flow systems of practical importance. More importantly, Tretheway and Leal [Tretheway and Leal, 1999] showed that polymers in a viscoelastic liquid exhibit surfactant effects, but that these effects are not associated with the water soluble polymers. In addition, surfactant may also

be added separately to the system to manipulate the flow. To the best of our knowledge, the combined effects of viscoelasticity and soluble surfactant have not been throughly investigated. The vast presence of surfactants in nature and also industrial applications on one hand and the significance and diversity of the polymers on the other hand make the study of the combined effects of surfactants and viscoelasticity a good scientific question that is worth studying. This study can also provide crucially important information and shed light on the physiology of the human respiratory system where surfactant is present in a mucus-like viscoelastic fluid in the airways and alveoli. In this respect, Lee et al. [Lee et al., 2011] used a flow focusing microfluidic device to quantify the effect of viscoelasticity on tip streaming phenomenon in the presence of surfactant. Later, Schenck and Fiegel [Schenck and Fiegel, 2016] carried out an experimental study to understand the effect of surfactant on a viscoelastic mucus-like fluid and how surface tension changes with surfactant and viscoelasticity. They investigated how the surface responds to surfactant in viscoelastic surfaces compared to clean aqueous systems. They showed that increasing the viscoelastic properties of the bulk fluid reduces the ability of surfactant to decrease the surface tension. The combined effects of surfactants and viscoelasticity are rarely studied. In particular, no computational work has been done for this purpose.

In the present study, we numerically investigate the combined effects of surfactant and viscoelasticity on a gravity-driven droplet rising or falling in an axisymmetric tube. The bulk and interface surfactant concentration coupled with the extra stresses are solved together with the incompressible Navier-Stokes equations using the finite-difference/front-tracking method developed by Muradoglu and Tryggvason [Muradoglu and Tryggvason, 2008]. The FENE-CR model is used to model viscoelasticity [Coates et al., 1992] while a Langmuir adsorption based non-linear equation of state is used to relate surface tension to the interfacial surfactant concentration [Levich, 1992]. In the front-tracking framework, both fluids are treated as a single fluid with discontinuous material properties and the effects of surface tension are taken into account by adding equivalent forces to the momentum equations in a conservative manner. The thesis is organized as follows: In chapter 2 the mathematical formulation of the two-phase flow is explained. In chapter 3 the front-tracking method and the employed strategies for solving the governing equations are explained. The results of our work are then discussed in chapter 4. In this chapter, gravity-driven droplets are studied

in a nearly-spherical, dimpled-ellipsoidal cap and skirted regimes. Finally, chapter 5 is the conclusion of this work where significant results are discussed. In this chapter, we also talk about the opportunities to extend this work in the future.

Chapter 2

MATHEMATICAL FORMULATION

In this chapter, the mathematical formulation is briefly described for a viscoelastic two-phase flow system in presence of soluble surfactant. All the equations are presented using a one-field formulation that is suitable for the front-tracking method. Following Unverdi and Tryggvason [Unverdi and Tryggvason, 1992], a single set of equations is written for the entire computational domain. In this formulation, the momentum conservation equations can be written in conservation form as

$$\begin{aligned}\frac{\partial \rho \mathbf{u}}{\partial t} + \nabla \cdot (\rho \mathbf{u}\mathbf{u}) &= -\nabla p + \nabla \cdot \mu_s(\nabla \mathbf{u} + \nabla \mathbf{u}^T) \\ &+ \Delta\rho \mathbf{g} + \nabla \cdot \boldsymbol{\tau} + \int_A \sigma(\Gamma)\kappa \mathbf{n}\delta(\mathbf{x} - \mathbf{x}_f)dA,\end{aligned}$$

where $\mu_s, \rho, g, p, \mathbf{u}$ and $\boldsymbol{\tau}$ represent fluid solvent viscosity, fluid density, the gravitational acceleration, pressure, velocity and viscoelastic extra stress tensor, respectively. The last term on the right hand side represents the body forces including the surface tension (σ) which is a function of interfacial surfactant concentration (Γ). In this term, κ is twice the mean curvature and $\mathbf{n}$ represents the normal vector to the interface. In the body forces term, a delta function is used because the surface tension only acts on the interface, the arguments of this function are the point at which the equation is evaluated ($\mathbf{x}$) and the point at the interface ($\mathbf{x}_f$) respectively. The flow is assumed to be incompressible so the mass conservation is given by

$$\nabla \cdot \mathbf{u} = 0. \tag{2.1}$$

We also assume that the material properties remain constant following a particle, i.e.,

$$\frac{D\rho}{Dt} = 0; \frac{D\mu_s}{Dt} = 0; \frac{D\mu_p}{Dt} = 0; \frac{D\lambda}{Dt} = 0, \tag{2.2}$$

where $\frac{D}{Dt}$ is the material derivative.

The surfactant concentration on the interface is defined as

$$\Gamma = \frac{dM_s}{dA}, \tag{2.3}$$

where M_s and A are the amount of surfactant adsorbed on the interface and the area of the droplet, respectively. The interfacial surfactant alters the surface tension according to the equation of state derived from the Langmuir adsorption [Wissler, 1963],

$$\sigma = \sigma_s + RT\Gamma_\infty \ln(1 - \frac{\Gamma}{\Gamma_\infty}), \tag{2.4}$$

where σ_s, R, T and Γ_∞ represent the surface tension of a clean interface, the ideal gas constant, the absolute temperature and the maximum packing concentration. Equation 2.4 can also be rewritten as

$$\sigma = \sigma_s[1 + \beta \ln(1 - \frac{\Gamma}{\Gamma_\infty})], \tag{2.5}$$

where $\beta = \frac{RT\Gamma_\infty}{\sigma_s}$ is the elasticity number. Following Muradoglu and Tryggvason [Muradoglu and Tryggvason Muradoglu and Tryggvason, 2014], Eq. 2.5 is slightly modified to avoid negative values of surface tension at large value of interface surfactant concentrations as

$$\sigma = \sigma_s \max[\epsilon_\sigma, 1 + \beta \ln(1 - \frac{\Gamma}{\Gamma_\infty})], \tag{2.6}$$

where ϵ_σ is a small value which is set to $\epsilon_\sigma = 0.05$ in this work. The interfacial surfactant concentration evolves by an advection-diffusion equation [Stone, 1990] in the form

$$\frac{\partial \Gamma}{\partial t} + \nabla_s \cdot (\Gamma \mathbf{U}_s) = D_s {\nabla_s}^2 + \dot{S}_\Gamma, \tag{2.7}$$

where U_s and D_s are the tangential velocity on the interface and the diffusion coefficient along the interface, respectively. The gradient operator along the interface is defined as

$$\nabla_s = \nabla - \mathbf{n}(\mathbf{n} \cdot \nabla). \tag{2.8}$$

In Eq. 2.7, $\dot{S}_\Gamma$ is the source term given by

$$\dot{S}_\Gamma = k_a C_s(\Gamma_\infty - \Gamma) - k_b \Gamma, \tag{2.9}$$

where k_a, k_b and C_s are the adsorption coefficient, the desorption coefficient and the surfactant concentration in bulk fluid adjacent to the interface, respectively. The bulk surfactant concentration evolves according to the following advection-diffusion equation

$$\frac{\partial C}{\partial t} = \nabla \cdot (C\mathbf{u}) + \nabla \cdot (D_{co} \nabla C), \tag{2.10}$$

where the molecular diffusion coefficient, D_{co}, is related to the molecular diffusivity of the surfactant in the bulk fluid as

$$D_{co} = D_C[1 - \mathbf{I}], \tag{2.11}$$

where $\mathbf{I}$ is the indicator function. The mass conservation of surfactant requires

$$\dot{S}_\Gamma = -D_{co}(\mathbf{n} \cdot \nabla C|_{interface}). \tag{2.12}$$

In this method, the total amount of mass adsorbed on the interface is distributed over the adsorption layer and added to the bulk concentration evolution equation as a negative source term in a conservative manner as suggested by Muradoglu and Tryggvason [Muradoglu and Tryggvason, 2008, Muradoglu and Tryggvason, 2014]. Equation (2.10) thus becomes

$$\frac{\partial C}{\partial t} = \nabla \cdot (C\mathbf{u}) + \nabla \cdot (D_{co}\nabla C) + \dot{S}_\Gamma. \tag{2.13}$$

2.1 Viscoelastic Stresses

The viscoelastic constitutive equations can be mathematically modeled and numerically solved. Viscoelastic models such as Oldroyd-B, FENE-CR and FENE-MCR can be written in a generic transport equation form as follows:

$$\frac{\lambda}{F}(\frac{\partial \mathbf{E}}{\partial t} + \nabla \cdot (\mathbf{uE}) - \nabla \mathbf{u}^T \cdot \mathbf{E} - \mathbf{E} \cdot \nabla \mathbf{u}) + \mathbf{E} = \mathbf{S}, \tag{2.14}$$

where $\mathbf{E}$ is the extra stress of conformation tensor and $F, \mathbf{S}$ and $\boldsymbol{\tau}$ are specified in table 2.1. In table .2.1, μ_p, $\lambda, L, F, \mathbf{I}$ and $\boldsymbol{\tau}$ are polymeric viscosity, relaxation time, the ratio of the length of a fully extended polymer dumbbell to its equilibrium length, stretch function, identity tensor and extra stress tensor respectively. The conformation tensor is defined as:

$$\mathbf{A} = \frac{\lambda}{\mu_p F}\boldsymbol{\tau} + \mathbf{I}. \tag{2.15}$$

In the present work, FENE-CR model is used for all the calculations.

Governing equations are solved in their dimensional form, and the results are expressed in terms of relevant non-dimensional form. Let $\mathcal{U}$ and $\mathcal{L}$ be appropriately defined velocity

Table 2.1: Specification of the parameters F, S and $\boldsymbol{\tau}$ in Eq.(2.14)

Model	F	**S**	$\boldsymbol{\tau}$
Oldroyd-B	1	**I**	$\mu_p F(\mathbf{E}\text{-}\mathbf{I})/\lambda$
FENE-CR	$Ł^2/(L^2 - trace(\mathbf{E}))$	**I**	$\mu_p F(\mathbf{E}\text{-}\mathbf{I})/\lambda$
FENE-MCR	$(L^2 + \lambda trace(\mathbf{E})/\mu_p)(L^2 - 3)$	$\mu_p(\nabla\mathbf{u} + \nabla\mathbf{u}^T)$	**E**

and length scales, respectively, and $t^* = \frac{\mathcal{L}}{\mathcal{U}}$ be the time scale, then governing non-dimensional numbers can be summarized as

$$Bi = \frac{k_b\mathcal{U}}{\mathcal{L}}; Da = \frac{\Gamma_\infty}{\mathcal{L}C_\infty}; Pe_c = \frac{\mathcal{U}L}{D_c}; Pe_s = \frac{\mathcal{U}L}{D_s}; \beta = \frac{\mathcal{R}T\Gamma_\infty}{\sigma_s}; \alpha = \frac{\mu_s}{\mu_s + \mu_p}; Wi = \frac{\lambda V^*}{d_d},$$

where Bi, Da, Pe_c, Pe_s, β, α and Wi represent Biot number, Damkohler number, Peclet number based on bulk surfactant diffusivity, , Peclet number based on interface surfactant diffusivity, elasticity number, solvent viscosity ratio and Weissenberg number, respectively.

It's worth stressing that in practical applications it's not feasible to change polymeric viscosity without changing relaxation time or visa versa, but in this computational work, we assume that it's possible. Therefore, the effects of Weissenberg number (as a function of relaxation time) and solvent viscosity ratio (as a function of polymeric viscosity) are studied independently.

2.2 Numerical Method

The flow equations (Eq. 2.1-2.1), extra stresses (Eq. 2.14) and surfactant concentration equations (Eq. 2.10) are solved coupled on a uniform staggered grid. In this method, the whole domain is treated as a single flow with variable material properties. Marker points are connected to form the drop interface that is placed in a stationary Eulerian grid. The Lagrangian and Eulerian grid can be seen in Fig. 2.1. The marker points move with the flow velocity and the interface between two marker points is called front element. The front is used to update the discontinuous material properties. At each time step, as the drop moves, the front nodes location is also updated. Indicator function is defined according to

the front location, meaning that if the input coordinates of the indicator function is inside the front, the value is one, otherwise it's zero. The indicator function definition is as follows:

$$\mathbf{I}(r,z,t) = \begin{cases} 1 & \text{Inside bubble,} \\ 0 & \text{Bulk fluid,} \end{cases} \tag{2.16}$$

The following properties which change discontinuously across the interface are given by

$$\mu_p = \mu_{p,i}\mathbf{I} + \mu_{p,o}(1-\mathbf{I}), \qquad \mu_s = \mu_{s,i}\mathbf{I} + \mu s, o(1-\mathbf{I}), \tag{2.17}$$

$$\lambda = \lambda_i + \lambda_o(1-\mathbf{I}), \qquad \rho = \rho_i\mathbf{I} + \rho_o(1-\mathbf{I}), \tag{2.18}$$

where subscriptions "i" and "o" show inside and outside the droplet.
As the drop moves, the coordinates of the front marker points are updated in each time step and new coordinates are obtained. Droplet may deform in different regimes which means that the size of the front elements changes over time. When the droplet stretches, front element elongates which might not be able too resolve the interface adequately and can lead to coarse front grid and numerical errors. Compression of the droplet on the other hand, reduces the size of front elements which can cause additional computational cost. In order to overcome these difficulties, Lagrangian grid is restructured after moving at each time step. In this work, if a front element is smaller than a specified minimum values, one or more front marked nodes are removed. If a front element is larger than a maximum defined value, one or more front nodes are added to the front by splitting the front elements. Projection method is used to solve the flow equations on a staggered fixed Eulerian uniform Cartesian grid. As it's shown in Fig. 2.2, velocity is stored at the cell faces while the pressure, material properties and extra stresses are stored at the center of the cells. When advancing the solution from time step n to $n+1$, the front marker point location is updated as follows:

$$\mathbf{X}_p{}^{n+1} = \mathbf{X}_p{}^{n} + \Delta t \mathbf{V}_p{}^{n}, \tag{2.19}$$

where X_p and V_p are the coordinates of the front nodes and the velocity of the front nodes interpreted from the stationary Eulerian grid and superscripts n and $n+1$ denote the start and the end of the current time step respectively. Then the indicator function and material properties are updated accordingly. The momentum equation is then divided in two parts.

First, the pressure gradient is ignored and the unprojected velocity field is calculated. Then pressure field is calculated using the unprojected velocity and the incompressibility condition [Izbassarov and Muradoglu, 2015].

Viscoelastic constitutive equations are solved by the log-conformation method (LCM) [Fattal and Kupferma

which is completely explained by Izbassarov et al.

[Izbassarov and Muradoglu, 2015]. To solve the surfactant equations, Eq. 2.9 is solved on the Lagrangian grid and the value of source term is calculated on the surface and then distributed on the Eulerian grid in a conservative manner. Equation 2.13 is then solved on the stationary Eulerian grid the bulk concentration is stored at the pressure nodes [Tasoglu et al., 2008].

To solve the governing equations on the computational domain, numbering of the cells and the points in which different parameters are stored can be found in Fig. 2.2. Figure 2.3 shows how different parameters of grid size ares defined. In this work, Density is stored at pressure nodes. To calculate the density values which are not located at the pressure nodes, averaging is used.

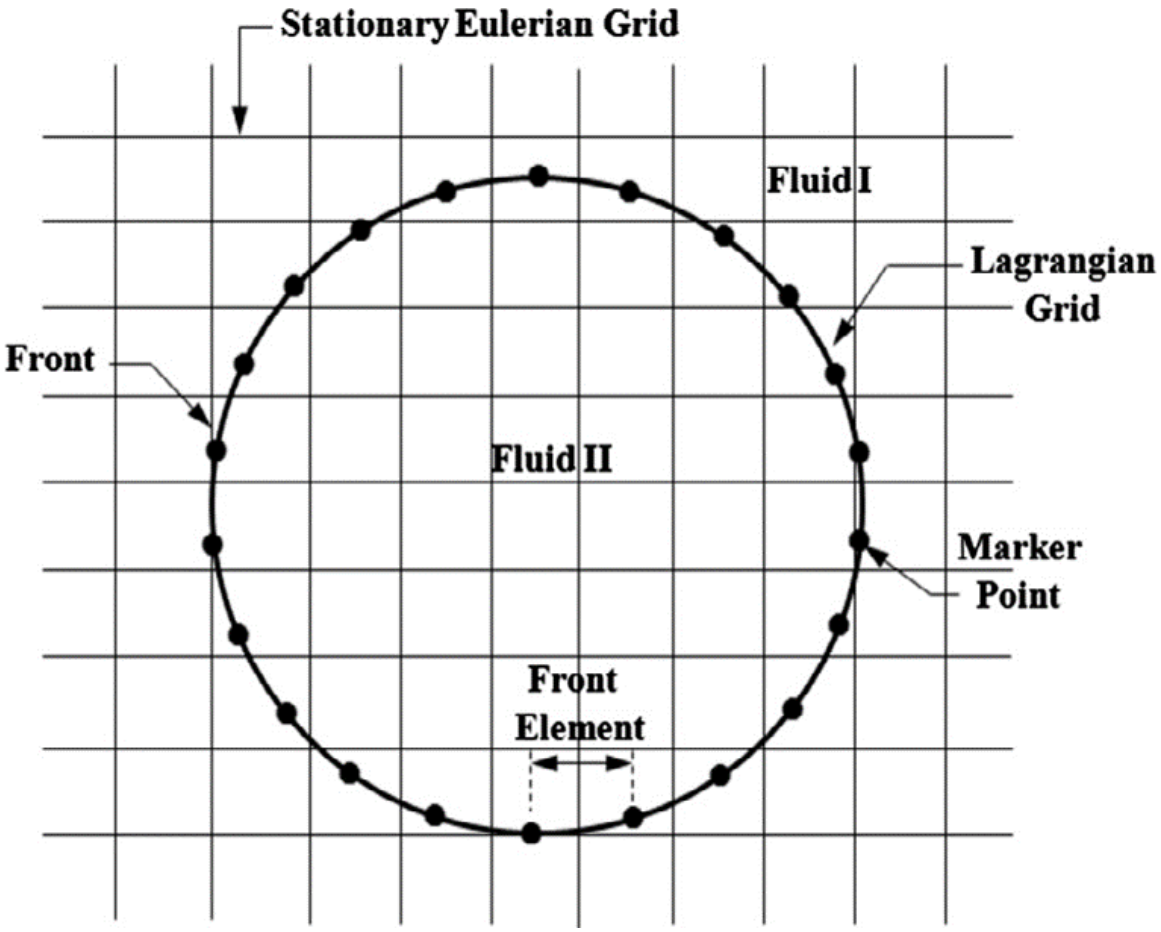

Figure 2.1: Schematic of the Stationary Eulerian grid and Lagrangian grid

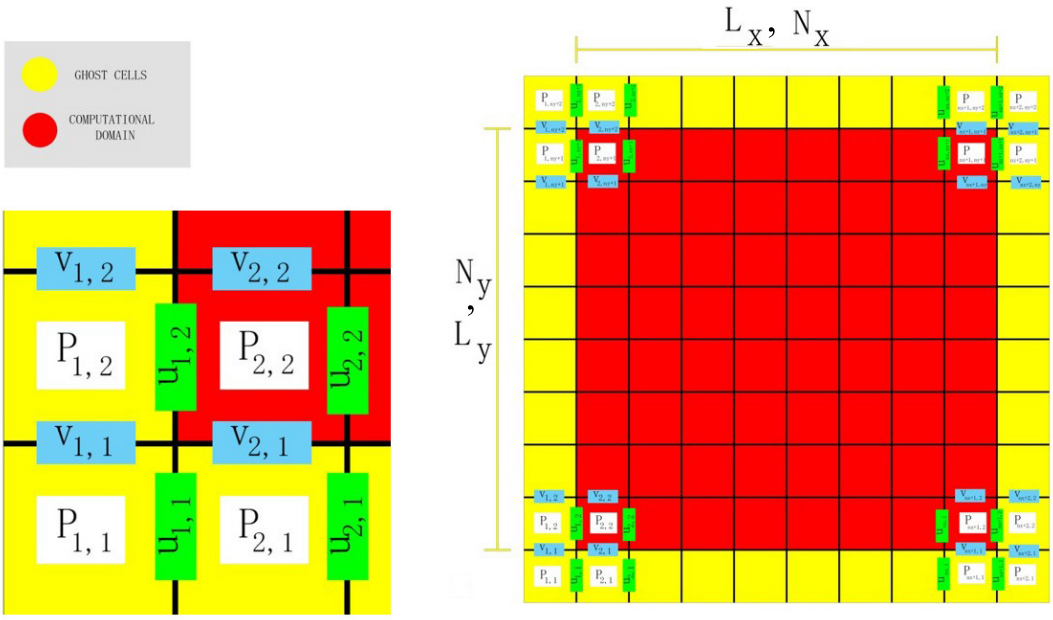

Figure 2.2: The used notation for a staggered grid where horizontal velocities are stored at the middle of the right and left edges of the cell and vertical velocities are stored at the middle of the top and bottom cells

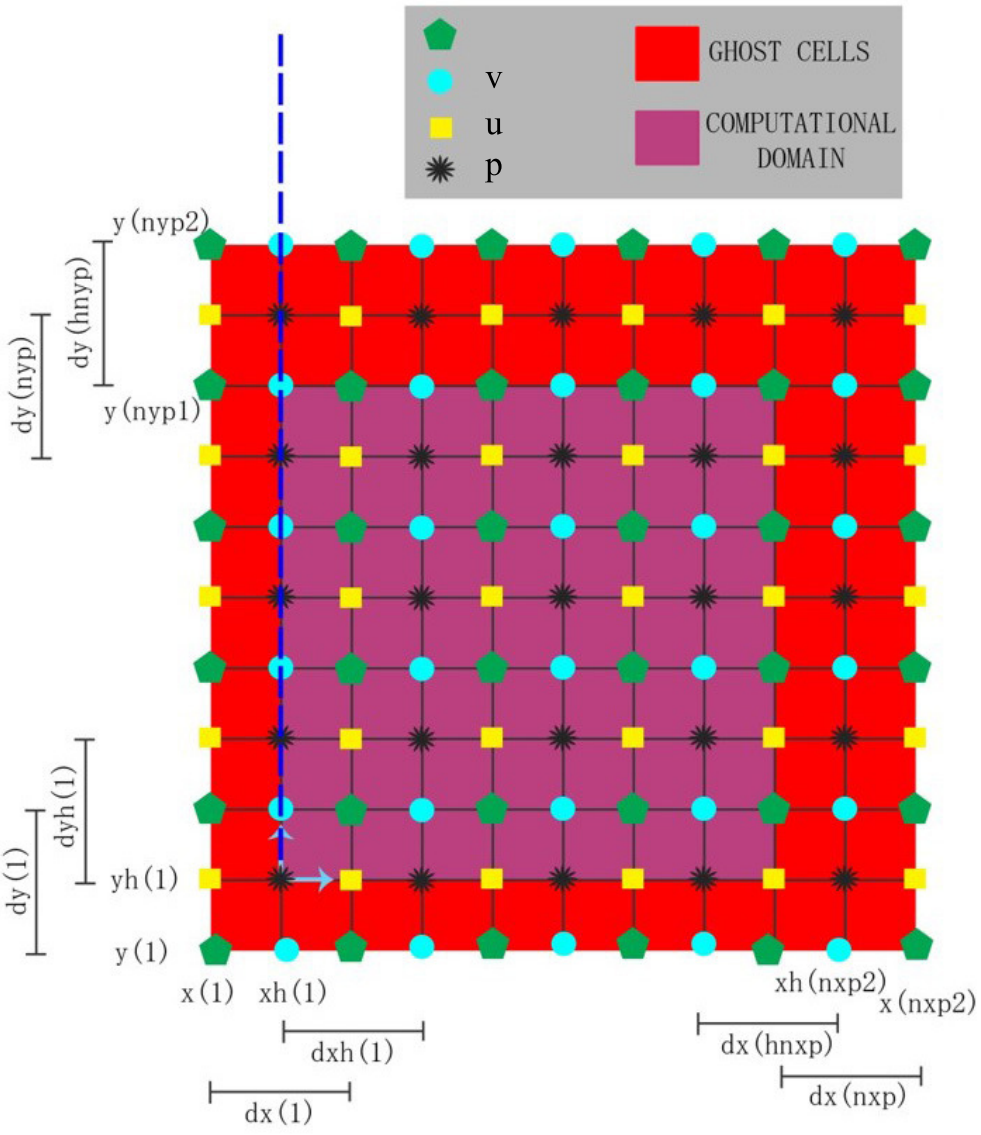

Figure 2.3: The notations used for the staggered grid, showing the relative positions where the pressure and velocities are stored.

Chapter 3

RESULTS AND DISCUSSION

Extensive simulations are performed and presented in this chapter. We consider a vertical tube of radius R and length L and assume that the flow is axisymmetric as sketched in Fig. 3.1. The tube is closed from both the bottom and the top ends. A spherical droplet of diameter d ($d < 2R$) is initially located at the centerline close to the bottom or the top walls depending on the direction of the gravitational force. It starts rising or falling in an otherwise quiescent liquid solely due to the gravitational force, i.e., the droplet is denser or lighter than the ambient fluid. The symmetry and the no-slip boundary conditions are applied at the centerline and the walls, respectively. The density ratio is set to $\rho_i/\rho_o = 0.5$ and $\rho_i/\rho_o = 2$ for the rising and falling droplet cases, respectively. Then the gravitational acceleration is varied to match desired flow conditions.

The droplet interface is assumed to be in an equilibrium with the bulk fluid, so the initial surfactant distribution is set to $\Gamma = \Gamma_{eq}$ where Γ_{eq} is determined based on the equilibrium conditions for $C_s = C_\infty$. The bulk fluid surfactant concentration is also initialized uniformly at $C = C_\infty$. The viscoelastic stresses are assumed to be zero.

In a purely gravity-driven flow, a droplet exhibits various flow regimes and takes various steady shapes mainly depending on the Eotvos (Eo) and Morton (Mo) numbers. The Eotvos and Morton numbers are defined as

$$Eo = \frac{\Delta\rho g d^2}{\sigma_s}, Mo = \frac{\Delta\rho g {\mu_o}^4}{{\rho_o}^2 {\sigma_s}^3}, \tag{3.1}$$

where $\Delta\rho$ is difference between the densities of the droplet and ambient fluids, g is the gravitational acceleration, σ_s is the surface tension of the clean interface and μ_o is the viscosity of the ambient fluid. A typical phase diagram is shown in Fig. 3.2 for a gravity-driven bubble/droplet moving in an unbounded ambient fluid [Clift et al., 2005]. As can be seen in this figure, the droplet motion can be broadly categorized into four main regimes at low Reynolds numbers: (i) The spherical or nearly spherical regime in which surface

tension forces dominate over the viscous forces. (ii) The ellipsoidal regime in which droplet takes an ellipsoidal shape due to significant viscous effects. (iii) The dimpled ellipsoidal-cap regime in which the droplet develops a dimple at its trailing edge. (iv) The skirted regime in which the dimple grows further and droplet takes a peculiar skirted shape as sketched in the figure. In this study, we do not consider high Reynolds number cases as the droplet exhibits significant three dimensional behavior that is not possible to resolve using present axi-symmetrical simulations. In the confined geometry as we consider here, all these regimes may not be realized due to significant wall effects. However, the phase diagram shown in Fig. 3.2 is still useful to select the parameters so that the combined effects of soluble surfactant and viscoelasticity can be examined in various flow regimes. In the present thesis, parameters are selected such the the resulting droplet motion resembles the nearly spherical, dimpled ellipsoidal-cap and skirted regimes for both rising and falling droplet cases. For this purpose, the Eotvos and the Morton numbers are set to $(Eo, Mo) = (1, 0.01), (50, 1250)$ and $(50, 5.7 \times 10^{-4})$ for the nearly spherical, the dimpled ellipsoidal-cap and a skirted droplet cases, respectively. These sets of parameters are marked in Fig. 3.2 by a blue plus sign, a black triangle and a green rectangle for the nearly spherical, the dimpled ellipsoidal-cap and a skirted droplet cases, respectively.

The Peclet, Damkohler and Biot numbers are kept constant at $Pe_s = 10, Pe_c = 100, Da = 32$ and $Bi = 20$ for all the results presented in this thesis. It is emphasized here that especially the Peclet numbers are much higher than these values in common physical systems and they are set to a much smaller value mainly for the numerical reasons, i.e., resolving thin mass boundary layer requires extremely fine grid that is impractical even in the present 2D simulations. The other parameters are varied to study the effects of viscoelasticity and soluble surfactant.

All the simulations are performed using a uniform Cartesian grid. Before presenting the computational results, we note that a comprehensive grid convergence study is performed and the results are summarized in the Appendix . As can be seen in the Appendix, a grid containing 64×640 cells in the radial and axial directions is found to be sufficient for obtaining grid-independent solutions. Therefore this grid is used in all the results presented in this this unless specified otherwise.

All the simulations are performed using dimensional quantities but the results are ex-

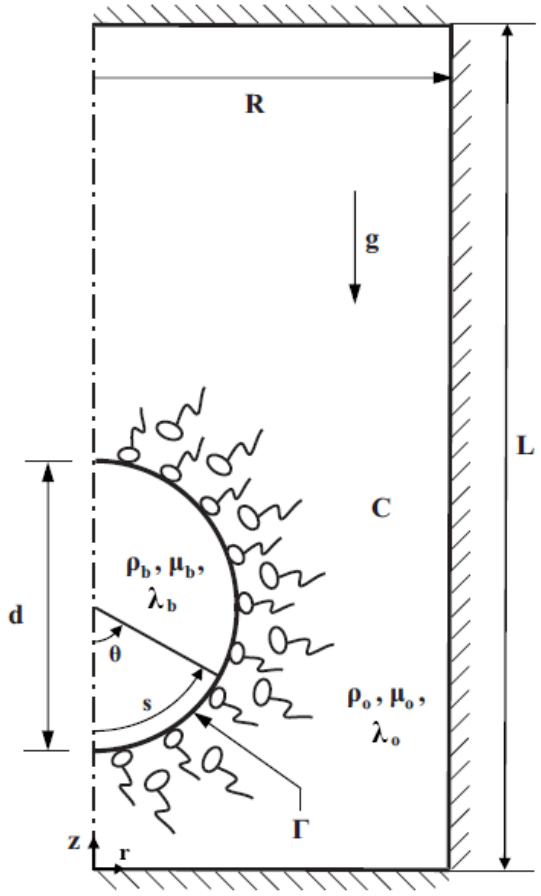

Figure 3.1: Schematic illustration of a gravity-driven viscoelastic droplet moving in an otherwise quiescent liquid containing a soluble surfactant in a closed circular tube.

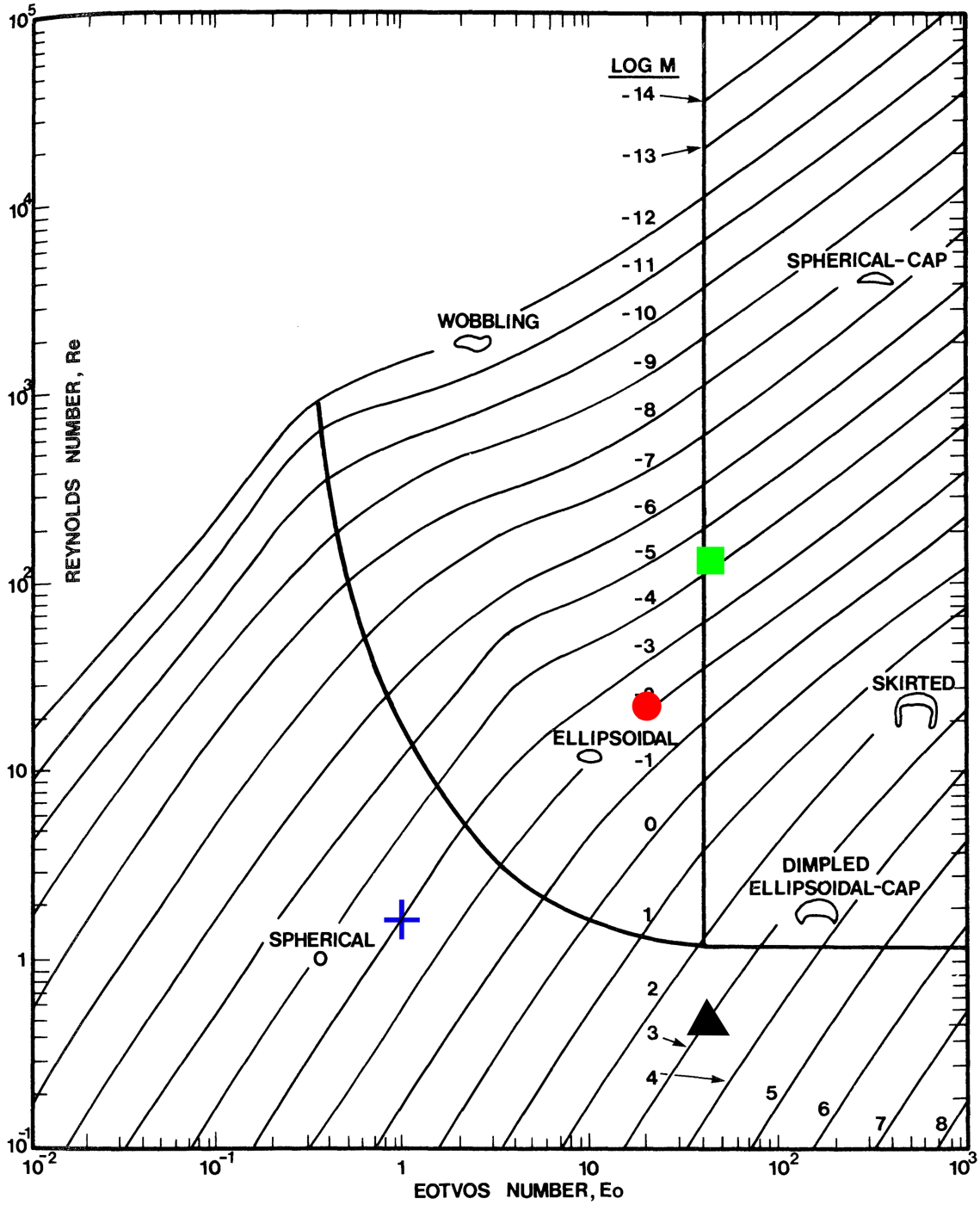

Figure 3.2: The phase diagram for various flow regimes and shapes of a gravity-driven bubble/droplet in an unbounded and otherwise quiescent liquid. Adopted from Clift et al. [Clift et al., 2005].

pressed in non-dimensional forms. For non-dimensionalization, the equivalent droplet diameter is used as a length scale, i.e, $\mathcal{L} = d$. For the velocity scale, we use the terminal velocity of an equivalent spherical droplet moving in an unbound fluid, i.e., $\mathcal{U} = U_{T\infty}$. The terminal terminal velocity was first obtained independently by Hadamard and Rybczynski in 1911 and is given by [Clift et al., 2005]

$$U_{T\infty} = \frac{2}{3}\frac{ga^2\Delta\rho}{\mu_{s,o}}\frac{\mu_{s,o}+\mu_{s,i}}{2\mu_{s,o}+3\mu_{s,i}}, \tag{3.2}$$

where $a = d/2$ is the radius of the droplet. We note that the terminal velocity of the droplet is significantly smaller than that given in Eq. (3.2) mainly due to the presence of the tube walls but also due to retardation effects of the surfactant as will be discussed later. The time scale is then obtained as $\mathcal{T} = d/U_{T\infty}$.

3.1 Combined effects of surfactants and viscoelasticity on a droplet rising in a denser fluid

We first consider the falling droplet case in which the droplet fluid is denser than the ambient fluid. Simulations are performed for three regimes.

3.1.1 Nearly spherical droplet rising in a denser fluid

Simulations are first performed for the nearly spherical regime. For this purpose, the Eotvos and Morton number are set to $Eo = 1$ and $Mo = 0.01$, respectively. A base case is designated to facilitate a systematic examination of effects of viscoelasticity and surfactant and the parameters are specified as $Pe_s = 10, Pe_c = 100, Da = 32$, $Bi = 20$, $\beta = 0.5$, $Wi = 50$ and $\alpha = 0.77$ for the base case in the nearly spherical regime.

First, the effects of surfactant are studied on a viscoelastic droplet rising in a tube due to buoyancy forces. Figure 3.3(a) shows the shape of the droplet and distribution of surfactant concentration at the interface (left side). The interfacial surfactant concentration is plotted against arclength in Fig. 3.3(b) where arclength is measured from the centerline in the counterclockwise direction. This figure shows that surfactant is convected along the interface and accumulates at the trailing edge of the droplet. The non-uniform distribution of the interfacial surfactant concentration results in a gradient of surface tension along the interface which in turn induces Marangoni stresses that counteract the viscous shear stresses

to reduce the mobility of the interface and thus increase drag force and reduce the terminal velocity of the droplet. This rigidification effect of surfactant is responsible for the complete immobilization of the interface in extreme cases in which the droplet behaves like as solid sphere [Tasoglu et al., 2008]. To show the effects of surfactant, the terminal velocity of the droplet is plotted against time in Fig. 3.4 for various values of elasticity number ranging between $\beta = 0$ and $\beta = 1$. It is clearly seen in this figure that the surfactant has a significant influence on the terminal velocity of a nearly spherical droplet, i.e., the terminal velocity decreases as β increases. However, the figure also shows that the reduction in terminal velocity gets smaller especially after $\beta \leq 0.5$. In other words, the terminal velocity becomes less sensitive to the changes in the elasticity number after a certain threshold value, i.e., there is no significant change in the terminal velocity for $\beta > 0.5$. This effect can be explained by the fact that the distribution of the interfacial surfactant concentration becomes more uniform as β increases as shown in Fig. 3.4(b). As a result, the Marangoni stresses remain nearly the same as β increases due to the reduction in gradient of the interfacial surfactant distribution. This is verified in Fig. 3.5 where the Marangoni stress is plotted as a function of the arclength for various values of the elasticity number. As seen, the Marangoni stress changes only slightly when the strength of surfactant is increased by two times. Therefore, the terminal velocity becomes less sensitive to variations in the elasticity number especially at higher values of β.

We now examine the effects of viscoelasticity in this case. The viscoelasticity is characterized by the Weissenberg number and solvent viscosity ratio. First, computations are performed for various Weissenberg numbers while keeping other non-dimensional numbers the same as in the base case. Figure 3.6 plots the constant contours of trace($\mathbf{B}$) which shows that the viscoelastic stresses remain uniform even for higher values of Weissenberg number. Then, the terminal velocity of the droplet is plotted versus non-dimensional time in Fig. 3.7 for various values of the Weissenberg number. It is clearly seen from this figure that the Weissenberg number does not have a significant influence on the drop dynamics in this regime. Then, further computations are performed for various solvent viscosity ratios. Figure 3.8 plots the constant contours of trace($\mathbf{B}$) where the viscoelastic stresses are uniform and increasing the solvent viscosity ratio has no considerable effect on the shape of the droplet. Figure 3.9 then plots terminal velocity versus non-dimensional time for various

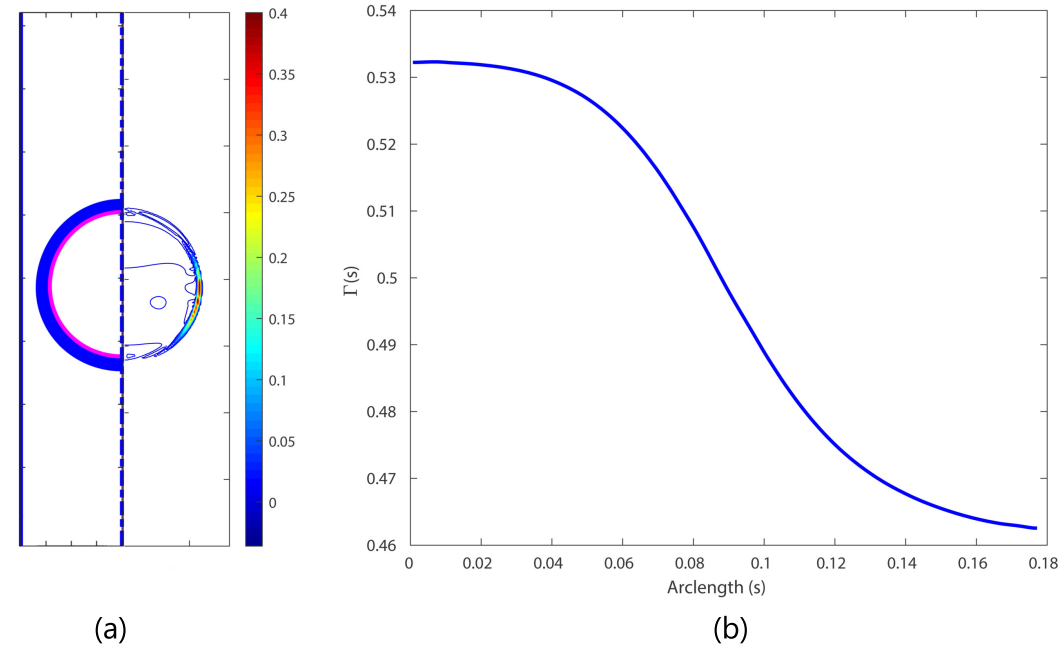

Figure 3.3: A nearly spherical droplet rising in a denser fluid. (a) The surfactant distribution and constant contours of $trace(\mathbf{B})$ plotted on and inside the droplet, respectively. (b) The interfacial surfactant concentration as a function of the arclength. $(\rho_i/\rho_o = 0.5, Eo = 1, Mo = 0.01, \alpha = 0.77, Wi = 50, \beta = 0.5, Grid : 64 \times 640)$.

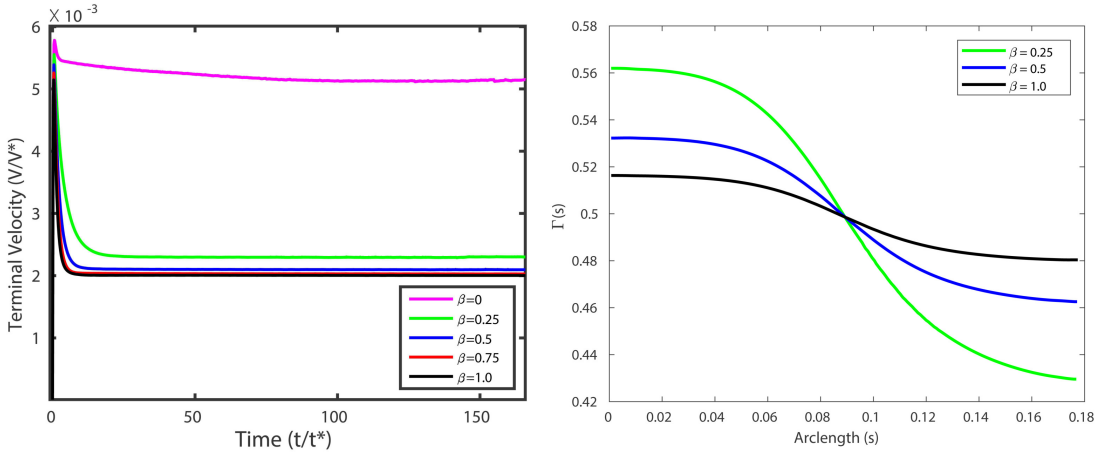

Figure 3.4: A nearly spherical droplet rising in a denser fluid. (a) Terminal velocity of the droplet versus non-dimensional time for various values of elasticity number ranging between $\beta = 0$ (clean) and $\beta = 1.0$ (highly contaminated). (b) The interfacial surfactant concentration as a function of the arclength for the same range of the elasticity number in (a). $(\rho_i/\rho_o = 0.5, Eo = 1, Mo = 0.01, \alpha = 0.77, Wi = 50, Grid : 64 \times 640)$.

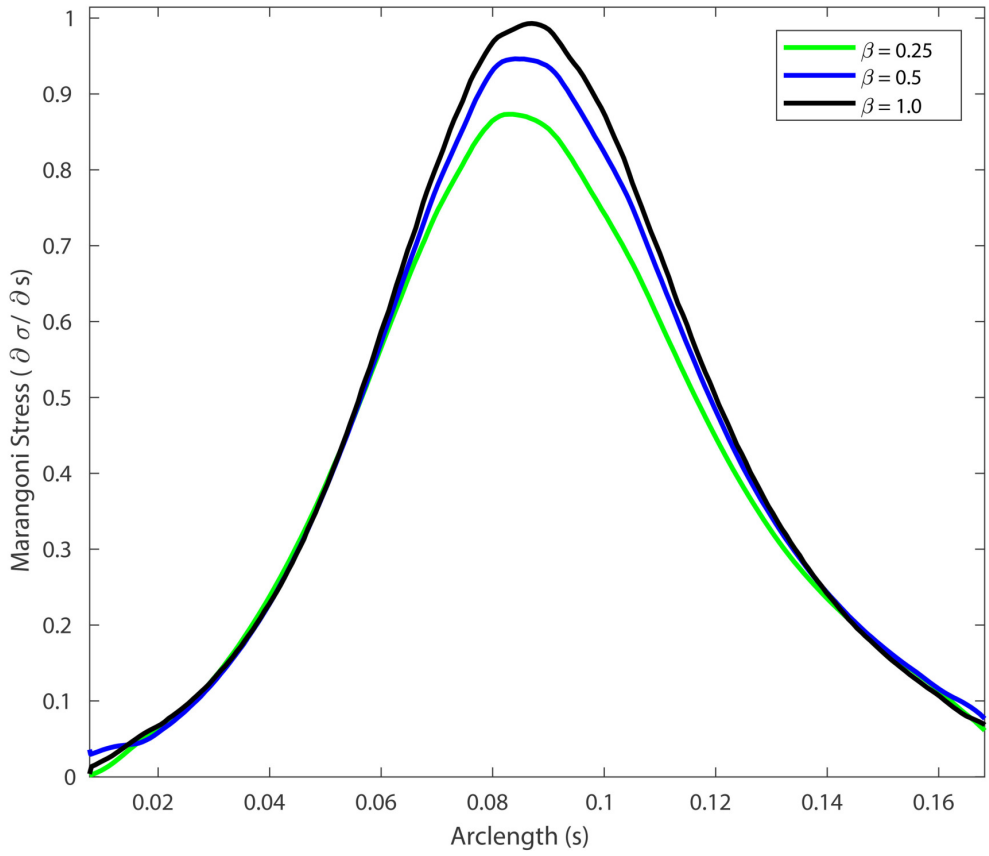

Figure 3.5: The Marangoni stress versus the arclength in the case of a nearly spherical droplet for various values of the elasticity number ranging between $\beta = 0$ (clean) and $\beta = 1.0(\rho_i/\rho_o = 0.5, Eo = 1, Mo = 0.01, \alpha = 0.77, Wi = 50, Grid : 64 \times 640)$.

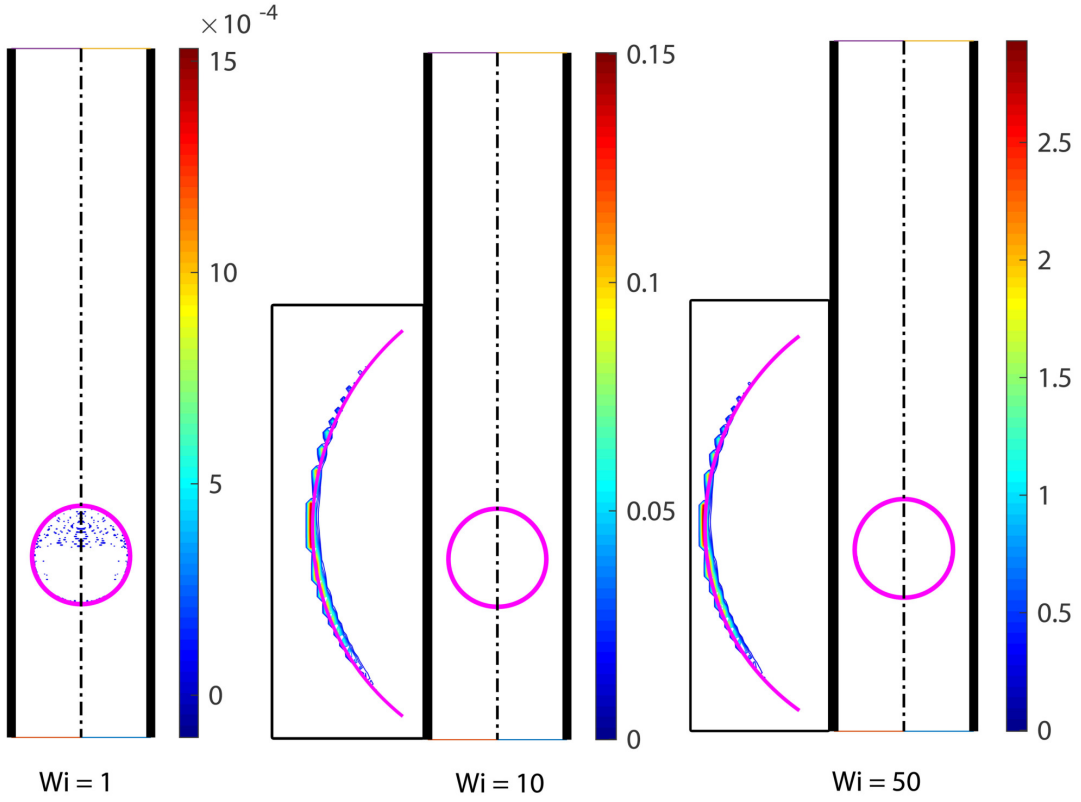

Figure 3.6: Constant contours of trace($\mathbf{B}$) for a nearly spherical droplet for various values of Weissenberg number. The magnified contours are also plotted for $Wi = 10$ and $Wi = 50$. ($\rho_i/\rho_o = 0.5, Eo = 1, Mo = 0.01, \beta = 0.5, \alpha = 0.77, Grid : 64 \times 640$).

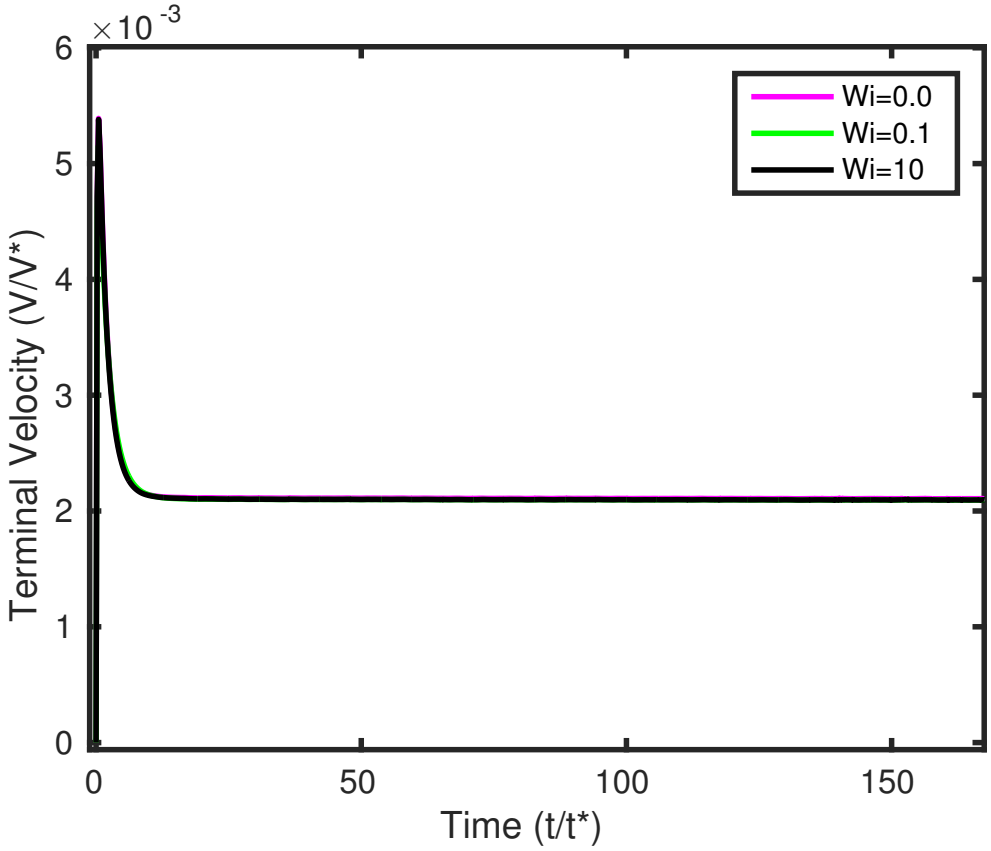

Figure 3.7: Effects of the Weissenberg number. The terminal velocity is plotted against the non-dimensional time for $Wi = 0$ (all Newtonian), $Wi = 0.1$ (mildly viscoelastic) and $Wi = 0.1$ (highly viscoelastic) cases. $(\rho_i/\rho_o = 0.5, Eo = 1, Mo = 0.01, \beta = 0.5, \alpha = 0.77, Grid : 64 \times 640)$.

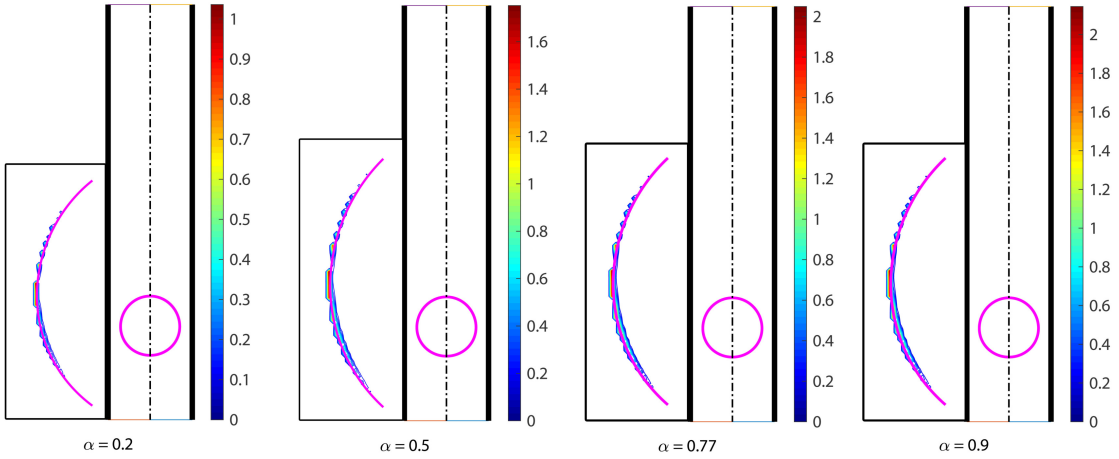

Figure 3.8: Constant contours of trace($\mathbf{B}$) for a nearly spherical droplet for various values of solvent viscosity ratio. ($\rho_i/\rho_o = 0.5, Eo = 1, Mo = 0.01, \beta = 0.5, Wi = 50, Grid : 64 \times 640$).

values of α. It shows that there is also no significant effect of solvent viscosity ratio on the dynamics of the droplet. It's important to note that $\alpha = 1$ shows the all Newtonian case. We thus conclude that the viscoelasticity does not have a significant influence on the terminal velocity of the droplet in the nearly spherical regime. This can be explained by the nearly uniform distribution of the viscoelastic stresses in the droplet as shown in Fig. 3.3(a) where the constant contours of the $\mathbf{B}_{zz}$ are plotted as a good measure of the viscoelastic stresses. This figure clearly shows that viscoelastic stresses are nearly uniform in this regime. Therefore, there is no significant effect of viscoelasticity on the dynamics of a nearly spherical droplet.

3.1.2 Dimpled-ellipsoidal cap droplet rising in a denser fluid

Simulations are then performed for a dimpled-ellipsoidal cap droplet case. For this purpose, the Eotvos and Morton numbers are set to $Eo = 50$ and $Mo = 1250$, respectively. We again designate a base by specifying the other parameters as $\rho_i/\rho_o = 0.5$, $Pe_s = 10$, $Pe_c = 100$, $Da = 32$, $Bi = 20$, $\beta = 0.5$, $Wi = 50$ and $\alpha = 0.77$. The effects of surfactant are characterized by the elasticity number since the bulk surfactant concentration has similar effects as does the bulk surfactant concentration. The effects of elasticity are characterized

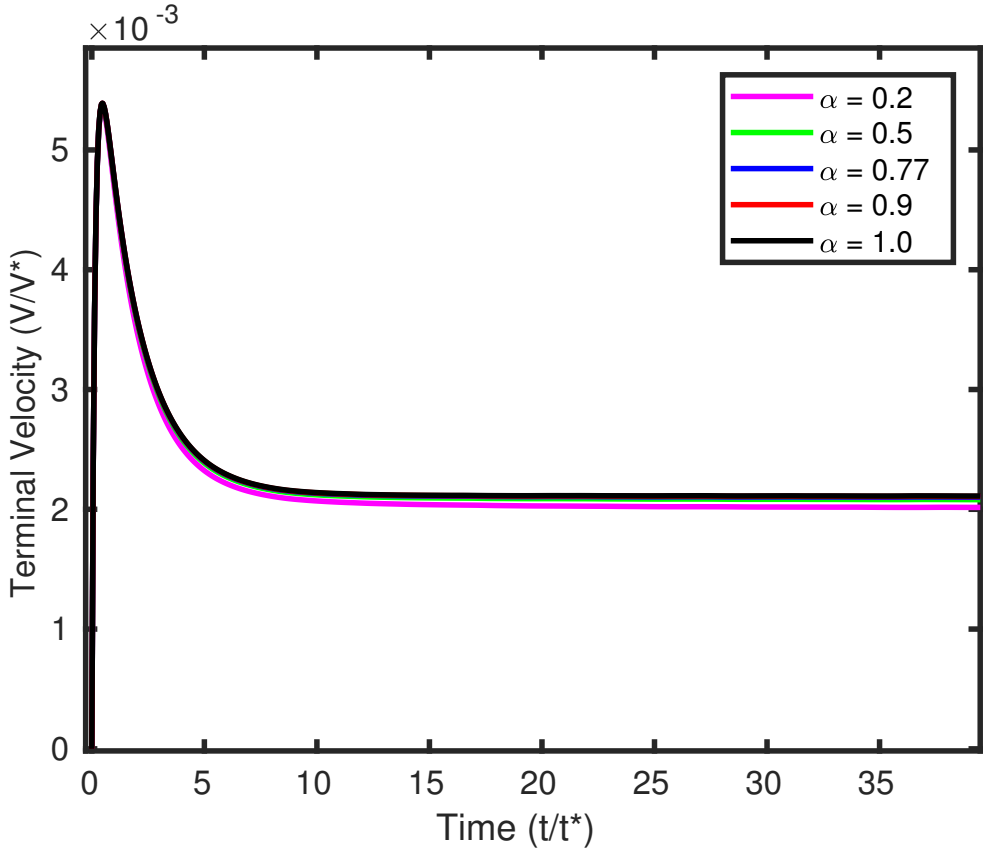

Figure 3.9: Effects of the the solvent viscosity ratio. The terminal velocity is plotted against the non-dimensional time for the solvent viscosity ratio ranging between $\alpha = 0.2$ and $\alpha = 0.9$. $(\rho_i/\rho_o = 0.5, Eo = 1, Mo = 0.01, \beta = 0.5, Wi = 50, Grid : 64 \times 640)$.

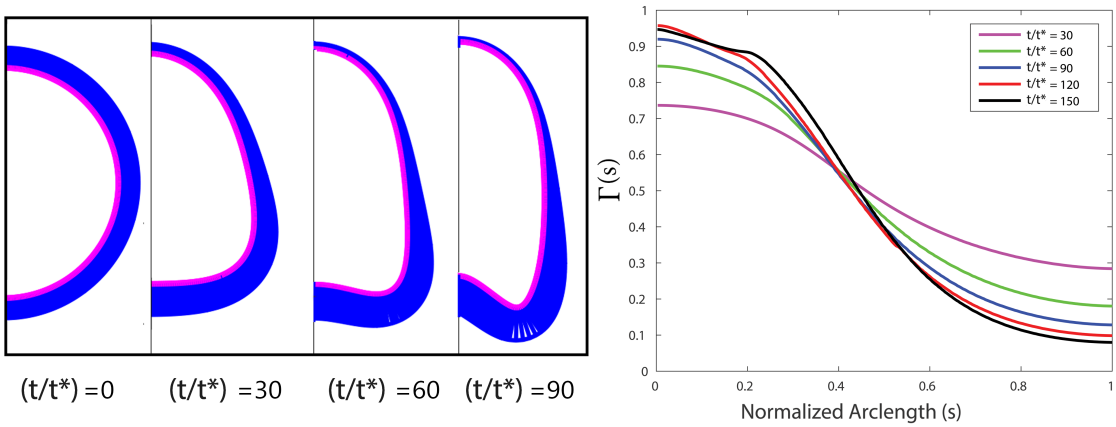

Figure 3.10: Time evolution of droplet shape and interfacial surfactant concentration distribution for a dimpled-ellipsoidal cap droplet rising in a denser fluid. (a) The droplet shape and the interfacial surfactant distribution at the droplet interface at the non-dimensional times $t/t^* = 0, 30, 60$ and 90. (b) The interfacial surfactant concentration as a function of the normalized arclength for a the same non-dimensional times as in (a). $(\rho_i/\rho_o = 0.5, Eo = 50, Mo = 1250, \alpha = 0.77, Wi = 50, Grid : 64 \times 640)$.

by the Weissenberg number and solvent viscosity ratio as before.

First, we investigate the effect of surfactant on the terminal velocity and shape of a viscoelastic droplet rising in a tube. For this purpose, computations are performed for different values of elasticity number while keeping the other parameters the same as in the base case. Figure 3.10 shows that the surfactant adsorbed at the leading edge is convected toward the trailing edge of the droplet and the surfactant gradient over the interface increases monotonically until a steady state is reached. This gradient in the interfacial surfactant induces significant Marangoni stresses that increase the drag force and reduce the terminal velocity of the droplet. The retardation effect of surfactant can be clearly seen in Fig. 3.11 where the time evolution of terminal velocity of droplet is plotted for $\beta = 0$ (clean) and $\beta = 0.5$ (contaminated) cases. It is also interesting to observe that surfactant has a weaker effect on the dynamics of a dimpled-ellipsoidal cap droplet compared to the nearly spherical droplet since the buoyancy-forces dominate over the surface tension forces in the dimpled-ellipsoidal cap case. In addition to the retardation of droplet, the contamination also affects the deformation of the droplet as shown in Fig. 3.12. In the all Newtonian case, the surfactant accumulation at the leading edge reduces the surface tension there, which

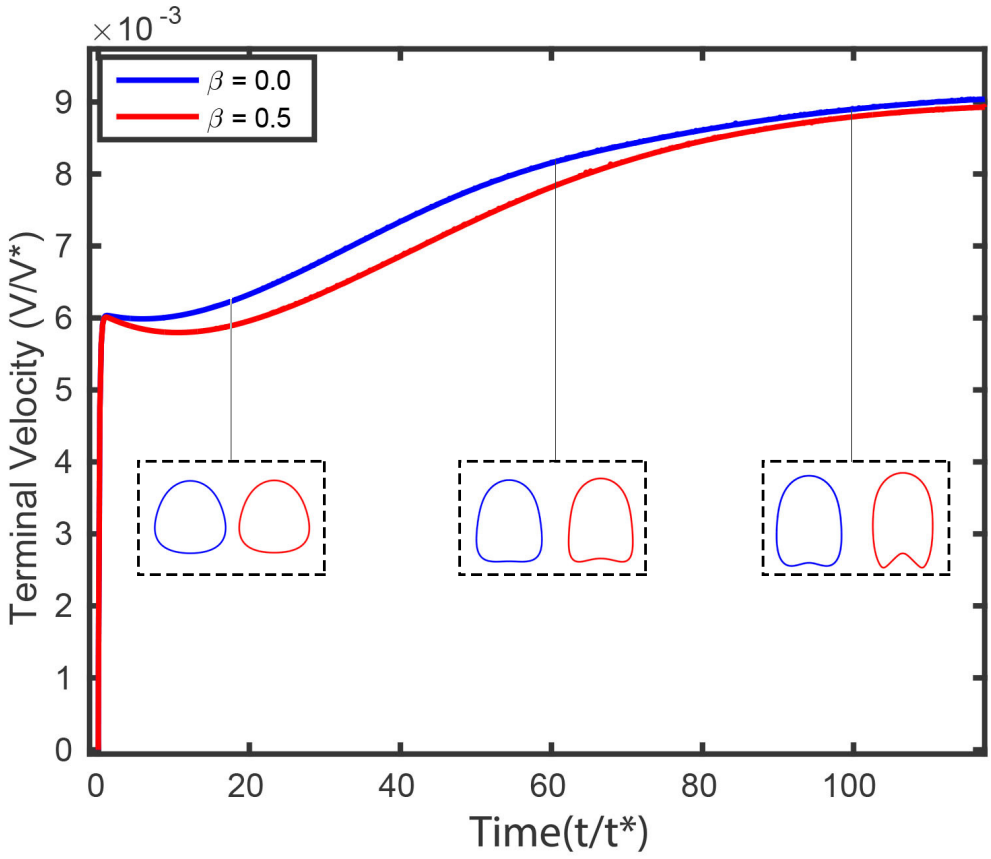

Figure 3.11: Time evolution of the terminal velocity and the shape of a clean ($\beta = 0$) and a contaminated ($\beta = 0.5$) droplet rising in a denser fluid in a dimpled-ellipsoidal cap regime ($\rho_i/\rho_o = 0.5, Eo = 50, Mo = 1250, \alpha = 0.77, Wi = 50, Grid : 64 \times 640$).

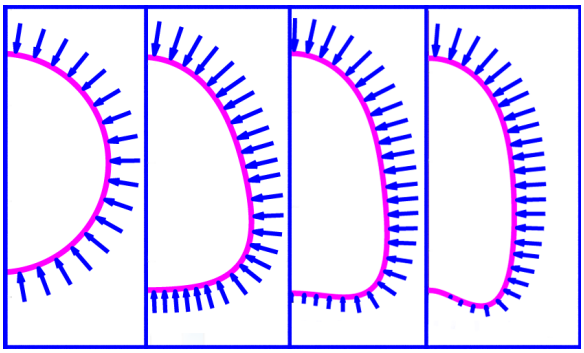

Figure 3.12: Distribution of the surface tension force on a dimpled-ellipsoidal cap droplet interface shown by arrows normal to the interface. The length of the arrows represents the magnitude of the surface tension force ($\rho_i/\rho_o = 0.5, Eo = 50, Mo = 1250, \alpha = 0.77, Wi = 50, \beta = 0.5, Grid : 64 \times 640$).

results in so-called tip streaming with an extended trailing edge. In the viscoelastic droplet case, however, the surfactant just reinforces the dimple already created by the viscoelastic stresses. As the strength of surfactant increases, the dimple penetrates further inside the droplet from the trailing edge. The effects of surfactant are summarized in Fig. 3.13 where the terminal velocity and deformation of the dimpled-ellipsoidal cap droplet are plotted against the non-dimensional time. As seen in this figure, the terminal velocity decreases while the deformation increases with the elasticity number. It is interesting to observe that, as the dimple penetrates further inside the droplet, the skirted edge of the dimple gets sharper, resembling the tip streaming phenomena. Although the present simulations are not capable of resolving the tip streaming, Fig. 3.13 suggests that the tip streaming is likely to occur not at the centerline but at the edge of the dimple away from the centerline.

Simulations are then performed to examine the effects of viscoelasticity on drop dynamics for this case. As mentioned before, the viscoelasticity is characterized by the Weissenberg number and solvent viscosity ratio. Thus we first examine the effects of the Weissenberg number. For this purpose, simulations are performed for a range of Wessenberg number between $Wi = 0$ (all Newtonian) and $Wi = 50$ (highly voscoelastic) while keeping the other parameters fixed at their values in the base case. Terminal velocity and steady shapes of the droplet are plotted in Figs. 3.15. As seen in this figure, the effect of Wi on terminal velocity is not monotonic, i.e., the terminal velocity decreases significantly when the

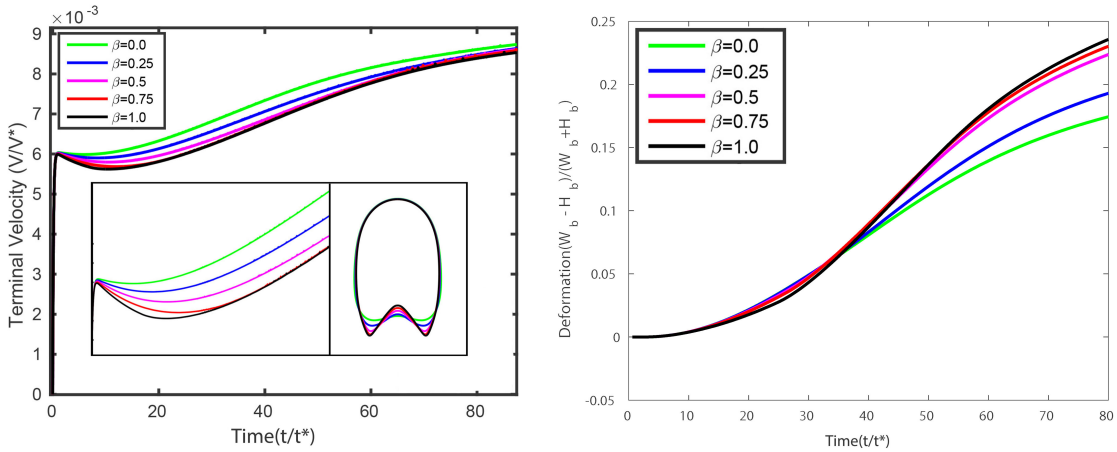

Figure 3.13: A dimpled-ellipsoidal cap droplet rising in a denser fluid. (a) Terminal velocity versus non-dimensional time and droplet shape for different elasticity numbers. (b) Deformation of the droplet as a function of time for various values of elasticity number in the range $\beta = 0$ (clean) and $\beta = 1$ (highly contaminated). $(\rho_i/\rho_o = 0.5, Eo = 50, Mo = 1250, \alpha = 0.77, Wi = 50, Grid : 64 \times 640)$.

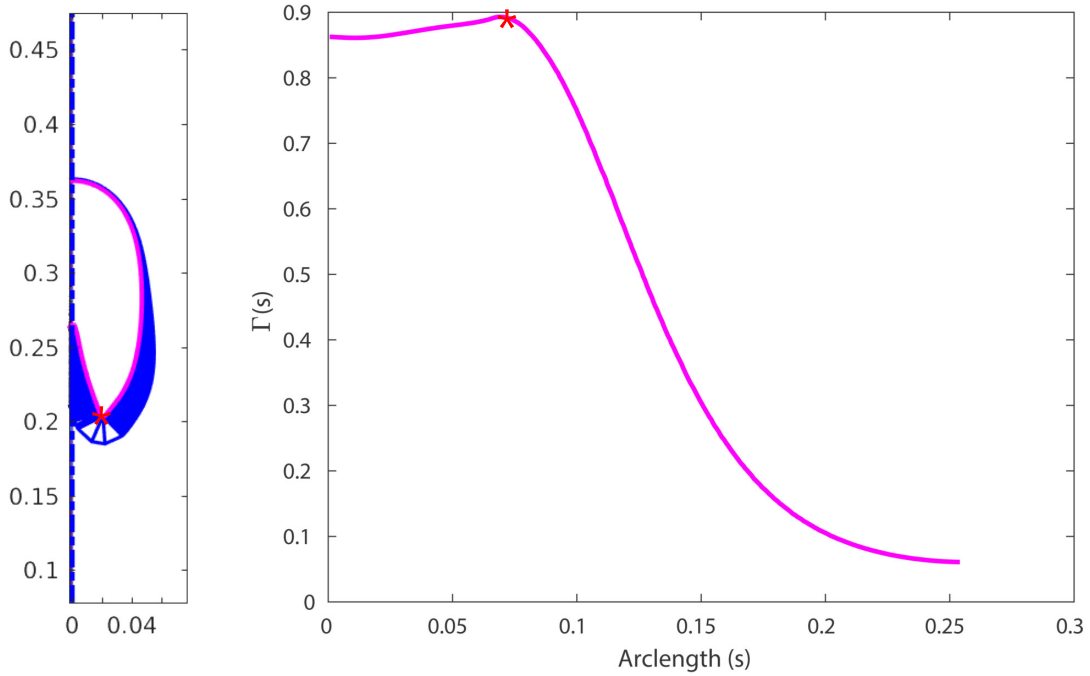

Figure 3.14: Droplet interface together with the interfacial surfactant concentration distribution (left) and the interfacial surfactant concentration plotted as a function of arclength at $t/t^* = 80$ for a dimpled-ellipsoidal cap droplet rising in denser fluid. $(\rho_i/\rho_o = 0.5, Eo = 50, Mo = 1250, \alpha = 0.77, Wi = 50, , \beta = 1, Grid : 64 \times 640)$.

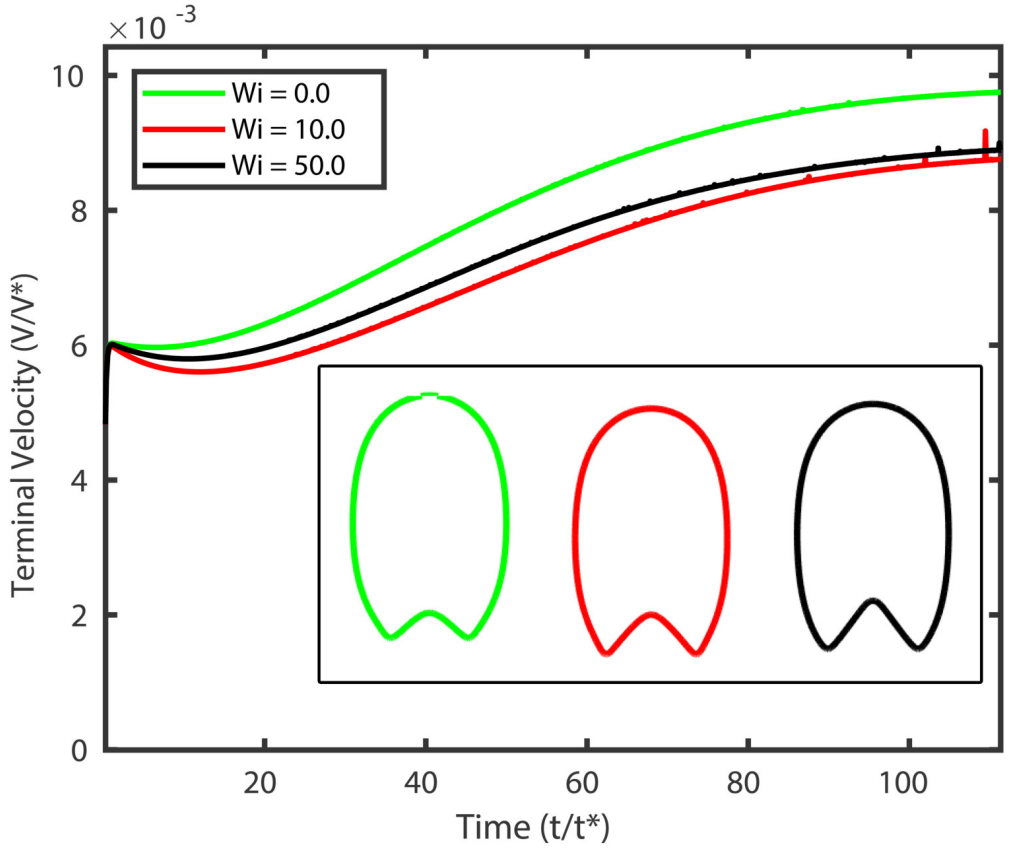

Figure 3.15: The time evolution of the terminal velocity and the shape of a dimpled-ellipsoidal cap droplet rising in a denser fluid for the Weissenberg numbers of $Wi = 0$ (all Newtonian), $Wi = 10$ (moderately viscoelastic) and $Wi = 100$ (highly viscoelastic). $(\rho_i/\rho_o = 0.5, Eo = 50, Mo = 1250, , \alpha = 0.77, \beta = 0.5, Grid : 64 \times 640)$.

Weissenberg number is increased up to $Wi = 10$ but a further increase in Wi results in slight increase in the terminal velocity. This interesting behavior can be partly attributed to enhanced deformation of the droplet at $Wi = 50$. The constant contours of $trace(\mathbf{B})$ are plotted in Fig. 3.16. This figure shows that the viscoelastic stresses are more concentrated at the trailing edge of the droplet near the centerline in the case of $Wi = 50$, which results in enhanced penetration of the dimple and thus more deformation. As droplet deforms, it becomes more extended in the axial direction and thus reduces the viscous drag.

We next examine the effects of the solvent viscosity ratio on drop dynamics in the dimpled-ellipsoidal cap case. For this purpose, the simulations are performed for the solvent viscosity ratio ranging between $\alpha = 0.5$ (highly viscoelastic) and $\alpha = 1$ (all Newtonian)

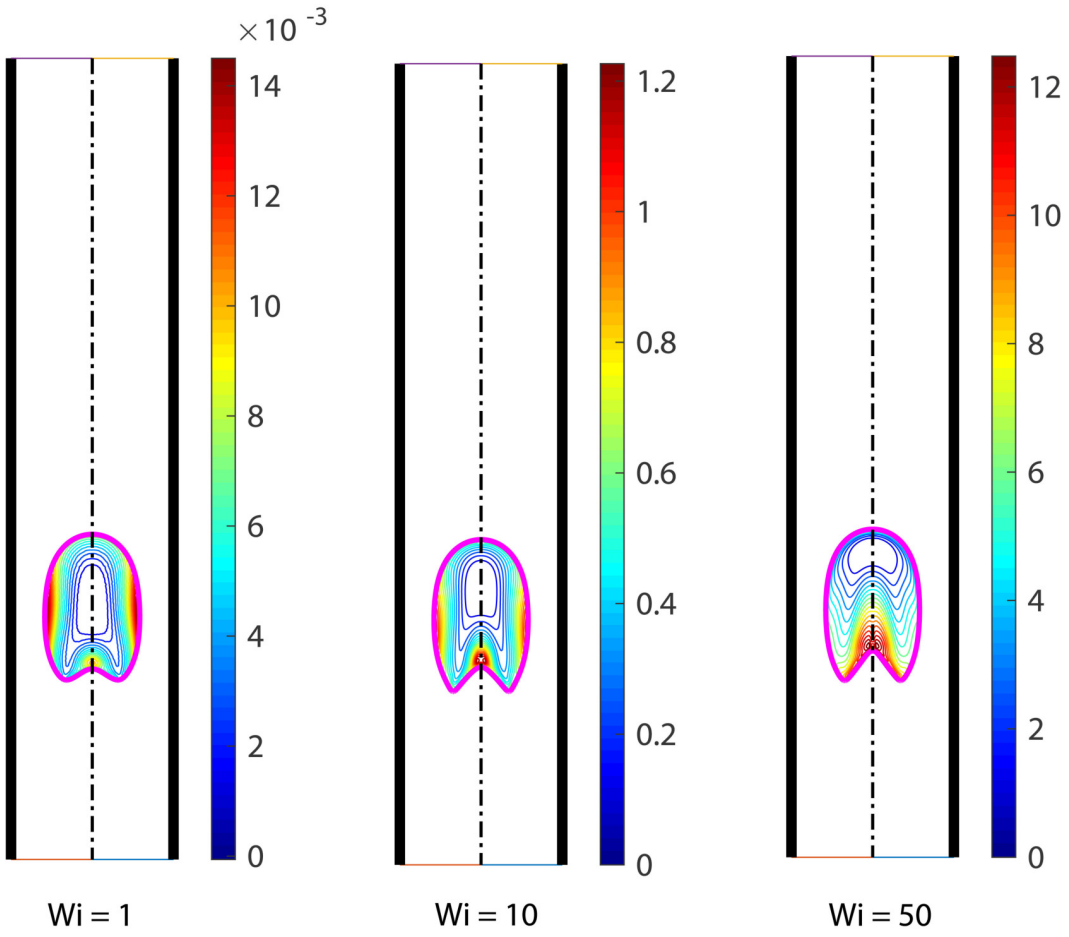

Figure 3.16: Constant contours of $trace(\mathbf{B})$ for a dimpled-ellipsoidal cap droplet rising in a denser fluid. $(\rho_i/\rho_o = 0.5, Eo = 50, Mo = 1250, , \alpha = 0.77, \beta = 0.5, Grid : 64 \times 640)$.

and the results are plotted in Fig. 3.17 and 3.18. Figure 3.17 shows the effects of the solvent viscosity ratio on the terminal velocity of droplet. As can be seen in this figure, the terminal velocity of droplet decreases significantly as the solvent viscosity ratio decreases or equivalently as the polymeric viscosity increases. This can be explained by the enhanced deformability of droplet at higher solvent viscosity ratios as shown in the inset of Fig. 3.17 where the steady shapes of the droplet are plotted for all the solvent viscosity ratios. As seen in the inset, the droplet deformability increases as α increases, which results in an increase in the terminal velocity. The constant contours of $trace(\mathbf{B})$ are also plotted in Fig. 3.18 for $\alpha = 0.5$, $\alpha = 0.77$ and $\alpha = 0.9$ when the droplet reaches a nearly steady state motion. This figure also shows that the viscoelastic stresses increase inside the droplet but the location of the viscoelastic stress concentration remains near the same as the solvent viscosity ratio increases. As a result of increased viscoelastic stresses concentrated at the trailing edge of the droplet near the centerline, the dimple grows and penetrates further inside the droplet as the solvent viscosity ratio increases, which in turn increases the deformation of the droplet.

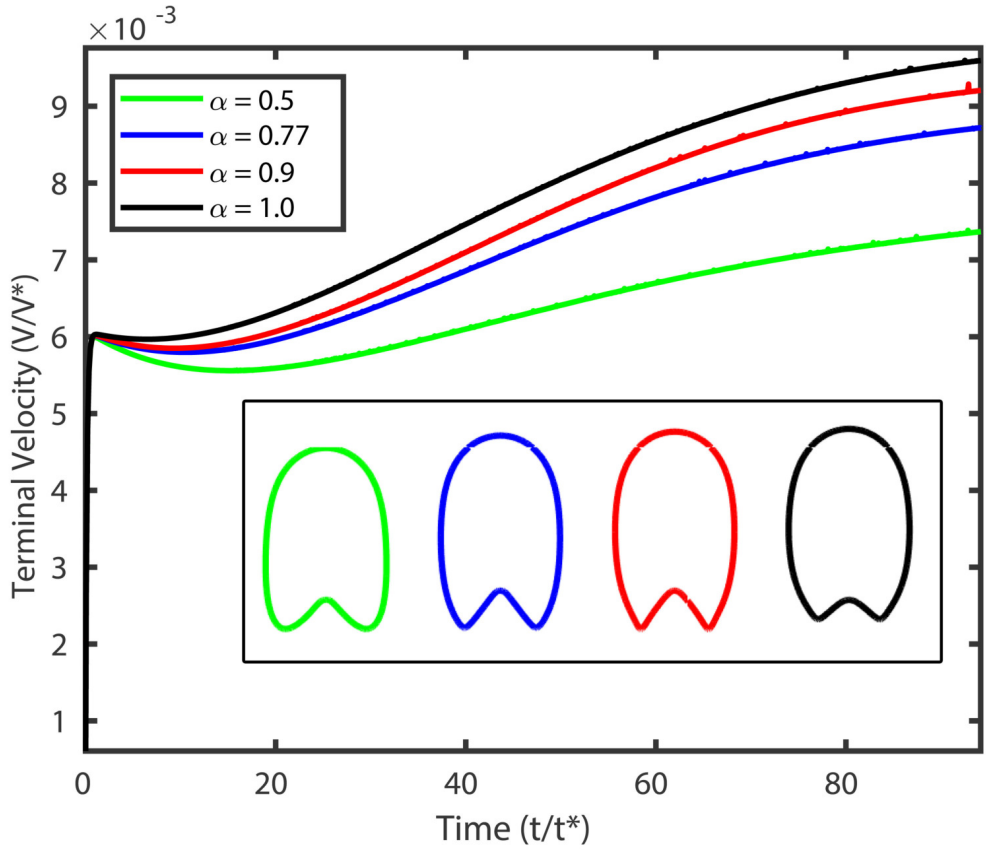

Figure 3.17: Terminal velocity versus non-dimensional time for different values of solvent viscosity ratio and shape of a dimpled-ellipsoidal cap droplet rising in a denser fluid ($\rho_i/\rho_o = 0.5, Eo = 50, Mo = 1250, , Wi = 50, \beta = 0.5, Grid : 64 \times 640$).

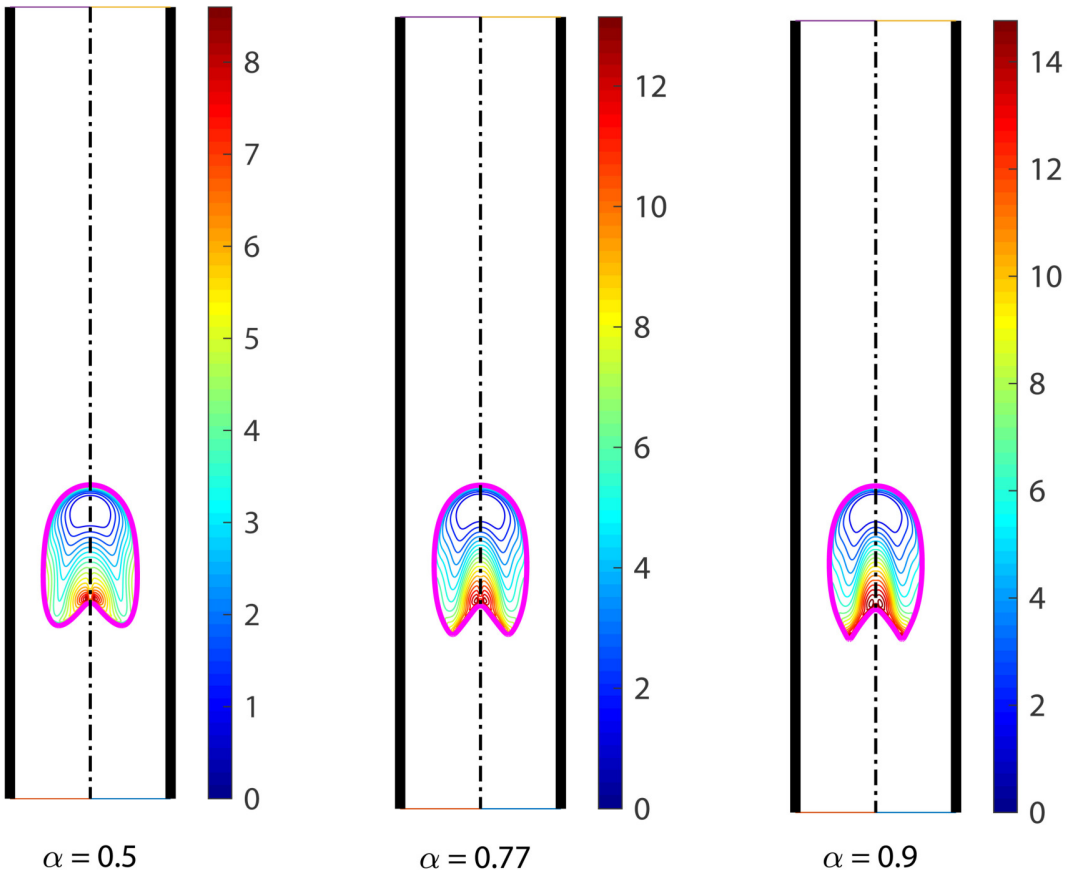

Figure 3.18: Constant contours of $trace(\mathbf{B})$ for a dimpled-ellipsoidal cap droplet rising in a denser fluid. (a) $\alpha = 0.5$. (b) $\alpha = 0.77$. (c) $\alpha = 0.9$. $(\rho_i/\rho_o = 0.5, Eo = 50, Mo = 1250, , Wi = 50, \beta = 0.5, Grid : 64 \times 640)$.

3.1.3 Skirted droplet rising in a denser fluid

In this section, we finally perform simulations to investigate the effects of surfcatant and viscoelasticity on drop dynamics for the skirted droplet. For this purpose, the Eotvos and Morton numbers are set to $Eo = 50$ and $Mo = 5.7 \times 10^4$, respectively. A base case is also designated for which the other parameters are set to $Pe_s = 1000$, $Pe_c = 10000$, $Da = 32$, $Bi = 0.05$, $\beta = 0.5$, $Wi = 50$ and $\alpha = 0.77$. First, we investigate the effect of surfactant on the terminal velocity and shape of a viscoelastic droplet rising in a tube. For this purpose, computations are performed for different values of elasticity number while keeping the other parameters constant.

We first examine effects of surfactant characterized by the elasticity number on drop dynamics in this regime. Simulations are performed for a range of the elasticity number between $\beta = 0$ (clean) and $\beta = 1$ (highly contaminated) and the results are shown in Fig. 3.19 where the evolution of the terminal velocity is plotted together with the shape evolution of droplet at various times. It is seen that the clean droplet eventually reaches a steady motion with a skirted shape. However, the contaminated droplets do not seem to attain a steady motion and the unsteadiness increases with β. It seems that the terminal velocity of droplet oscillates with a certain frequency in highly contaminated cases. This oscillatory behavior is mainly induced by the continuous penetration of dimple that eventually causes a hole at the center of the droplet as shown in the inset in Fig. 3.19. This interesting behavior is caused by the combined effects of surfactant and viscoelasticity: The viscoelastic stresses concentrate and cause a dimple at the trailing edge of the droplet, and surfactant reinforces this effect and makes the dimple larger and penetrate further into the droplet. Interfacial surfatant concentration is shown in Fig. 3.20 at time $t/t^* = 20$ for the case of $\beta = 0.5$. On the left side of Fig. 3.20, the surfactant concentration is represented by blue lines drawn normal to the interface. The length of lines indicates the magnitude of the surfactant concentration. As seen in this figure, the interfacial surfactant adsorbed at the leading edge is quickly convected toward the trailing edge at the interface and accumulates at the back of the droplet where it is released back into the bulk fluid. This can bee better seen on the right plot in Fig. 3.20 where the interfacial surfactant concentration is plotted as a function of the arc length measured from the centerline at the back of the droplet in counter clockwise direction. The stagnation point is marked by a star sign in both plots in Fig. 3.20. As

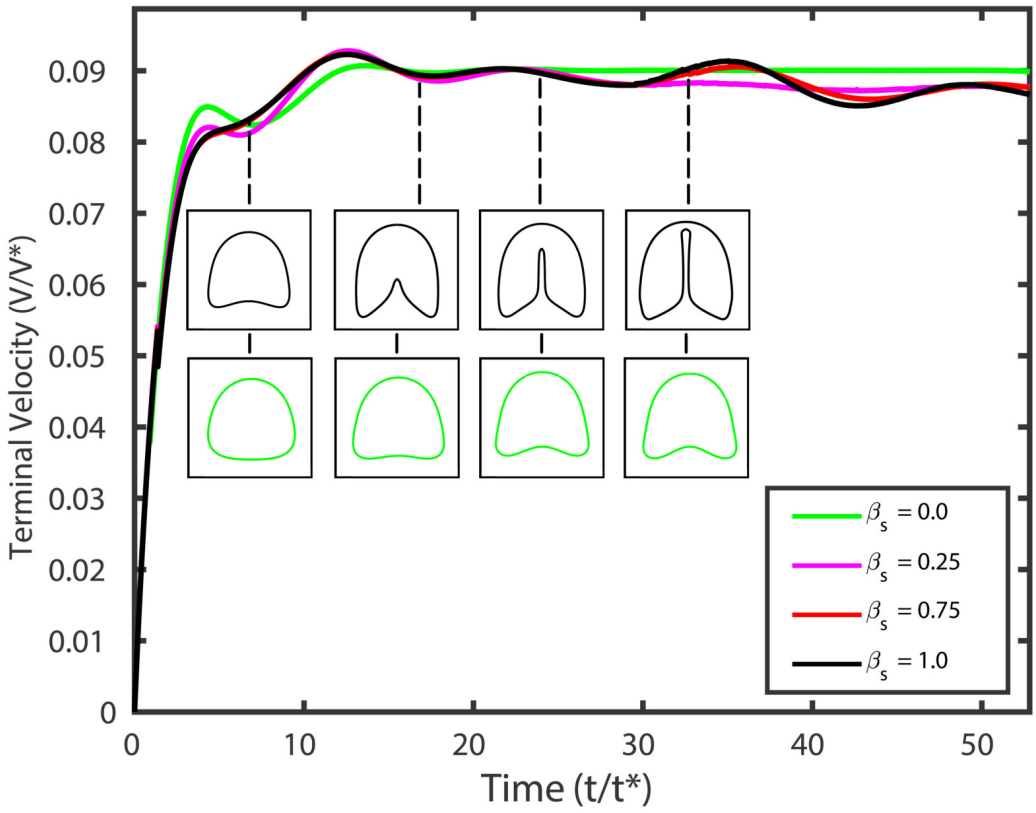

Figure 3.19: Time evolution of the terminal velocity and shape of a clean ($\beta = 0$) and contaminated ($\beta = 1$) skirted droplet rising in a denser fluid. ($\rho_i/\rho_o = 0.5, Eo = 50, Mo = 5.7 \times 10^{-4}, \alpha = 0.77, Wi = 50, Grid : 64 \times 640$).

can be seen in this figure, the surfactant concentration nearly reaches the maximum value of $\Gamma = 1$ at the back part of the droplet from the centerline up to the stagnation point, and then decreases quickly to make the leading edge of droplet nearly clean. It is known that tip streaming occurs when the surfactant concentration reaches the maximum value at the interface. As mentioned before, we cannot resolve the tip streaming phenomena in the present simulations mainly due to the lack of resolution. Nevertheless, Fig. 3.20 suggests that it is highly likely that tip streaming occurs near the stagnation point marked by a plus sign in the left plot of 3.20. More interesting, the figure also suggests that a tip streaming may also occur at the centerline towards inside the droplet provided that the surfactant is also soluble in the droplet liquid. Computations are then performed to study the effects of viscoelasticity on drop dynamics in the skirted droplet case. Figure 3.21 shows the effect of

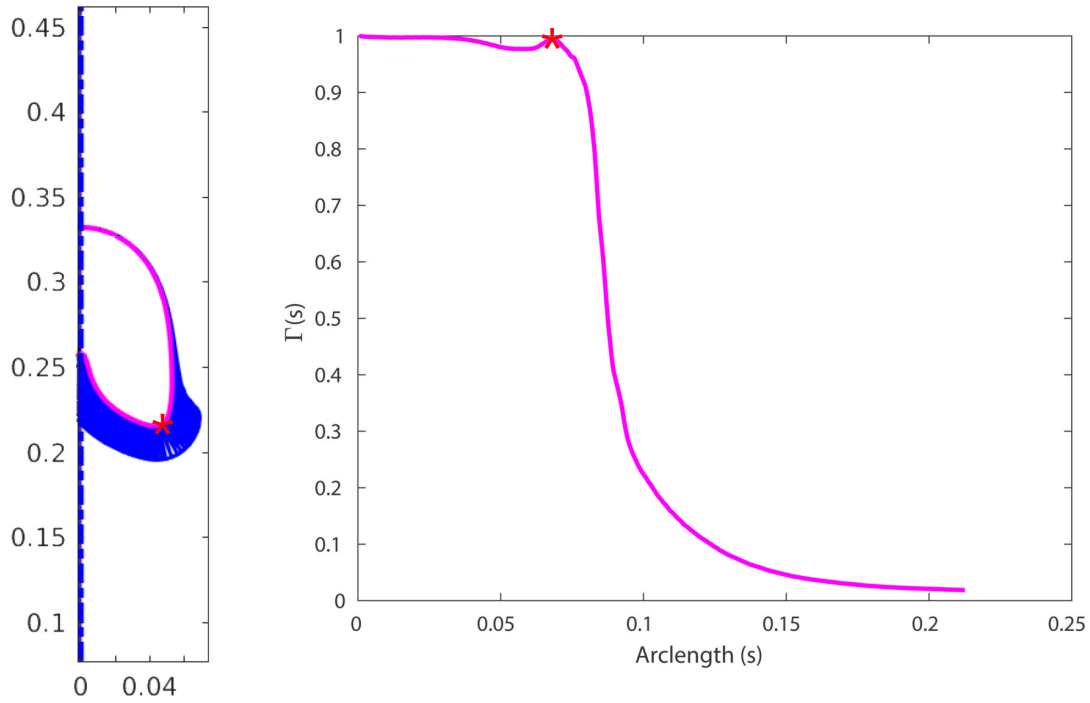

Figure 3.20: The droplet interface and the interfacial surfactant concentration at the interface (left plot) and interfacial surfactant distribution as a function of the arclength (right plot) at $t/t* = 20$ for a skirted droplet rising in denser fluid. ($\rho_i/\rho_o = 0.5, Eo = 50, Mo = 5.7 \times 10^{-4}, \alpha = 0.77, Wi = 50, \beta = 0.5, Grid : 64 \times 640$).

the Weissenberg number on the terminal velocity of a viscoelastic skirted droplet moving in a Newtonian fluid. As seen, the Weissenberg number dramatically affects the deformation and thus the terminal velocity of the skirted droplet. As Wi increases, the dimple at the back of the droplet grows rapidly, penetrates into the droplet and eventually creates a hole at the centerline. These results can be interpreted only qualitatively since the computational grid still not sufficient to fully resolve the flow especially near the penetration hole and breakup is not allowed in the present implementation. Furthermore, the flow may not be axisymmetric for this case. Figure 3.22 depicts the constant contours of $trace(\mathbf{B})$ at non-dimensional time ($t/t^* = 8$). This figure shows that the viscoelastic stresses are pronounced close to the center line. Note that, as Wi increases, the penetration happens earlier. At the highest Weissenberg number of $Wi = 500$ considered in this study, the dimple penetrates quickly and a hole is created at the center of the droplet at the non-dimensional time of $t/t^* = 13$.

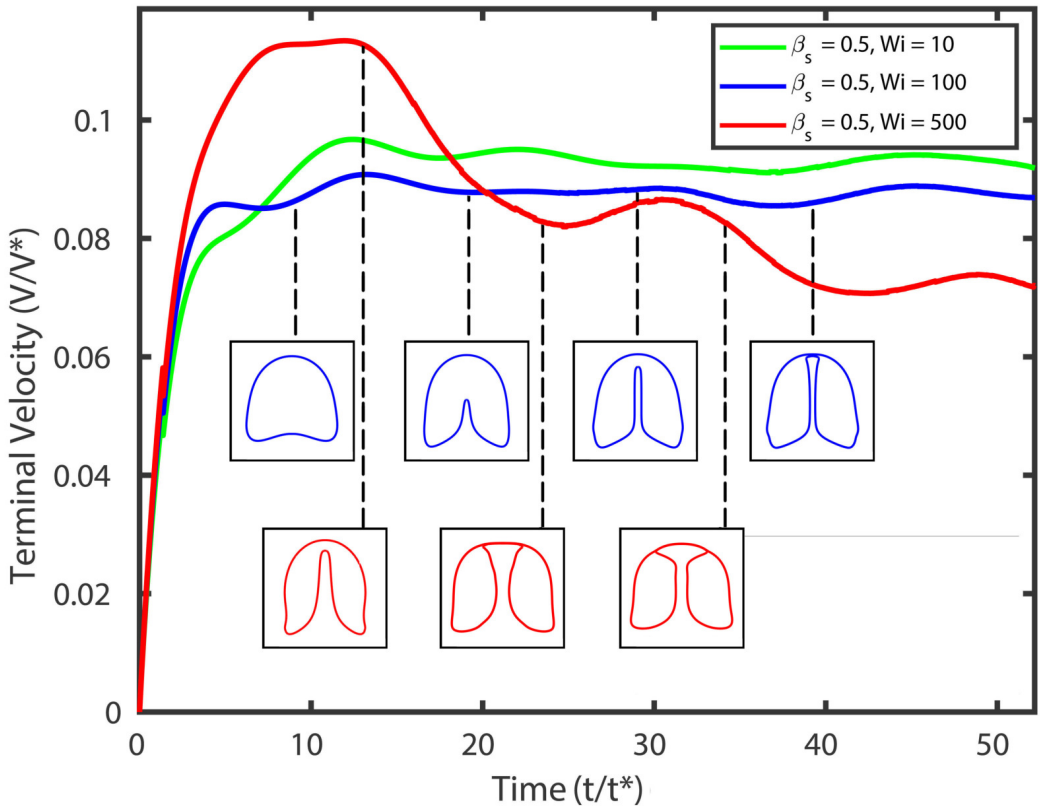

Figure 3.21: Time evolution of the terminal velocity and the shape evolution of a contaminated skirted droplet rising in a denser fluid computed for $Wi = 0$, $Wi = 100$ and $Wi = 500$. $(\rho_i/\rho_o = 0.5, Eo = 50, Mo = 5.7 \times 10^{-4}, \alpha = 0.77, \beta = 0.5, Grid : 64 \times 640)$.

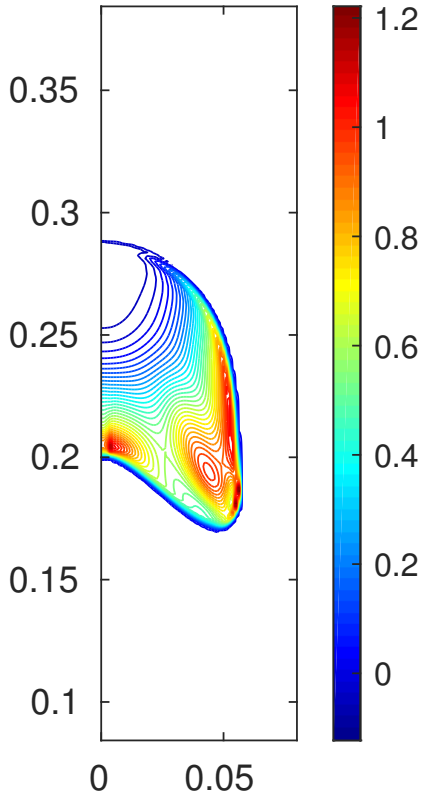

Figure 3.22: Constant contours of the $trace(\mathbf{B})$ for a contaminated skirted droplet at the non-dimensional time $t/t^* = 8$ ($\rho_i/\rho_o = 0.5, Eo = 50, Mo = 5.7 \times 10^{-4}, \alpha = 0.77, Wi = 50, \beta = 0.5, Grid : 64 \times 640$).

3.2 Combined effects of surfactant and viscoelasticity on a droplet falling in a less dense fluid

In this section, a droplet falls in a less dense fluid. The droplet moves downward because of the gravity forces where $\rho_i/\rho_o = 2$. Nearly spherical, dimpled-ellipsoidal cap and skirted droplets are studied in this regime. First, a nearly spherical droplet is studied where $Eo = 1$ and $Mo = 0.01$. This regime is specified on Fig. 3.2 via a blue plus sign. Then, a dimpled-ellipsoidal cap droplet is investigated for which $Eo = 50$ and $Mo = 1250$, this regime is specified on Fig. 3.2 with a black triangle. Finally, a skirted droplet with $Eo = 20$ and $Mo = 0.01$ is studied which is shown with a red square on Fig. 3.2.

3.2.1 Nearly spherical droplet falling in a less dense fluid

In this regime, computations are performed by keeping the non-dimensional numbers constant at $Pe_s = 10000, Pe_c = 100000, Da = 32$, $Bi = 0.02$, $\beta = 0.5$, $Wi = 50$ and $\alpha = 0.77$. The *Eötvös* number and Morton number have values $Eo = 1$ and $Mo = 0.01$ respectively, where a clean droplet is expected to be in a nearly spherical regime. First, we investigate the effects of surfactant on the terminal velocity and shape of a viscoelastic droplet rising in a tube. For this purpose, computations are performed for different values of elasticity number while keeping the other parameters fixed.

When the droplet falls in a less dense fluid, surfactants start convecting to the trailing end, this can be seen in Fig. 3.23. The aggregation of surfactant at the trailing edge creates a gradient of surfactant which in turn induces Marangoni stresses. The terminal velocity reduces as a result of the Marangoni stresses. Figure 3.24 shows the terminal velocity versus non-dimensional time for different values of elasticity number. It's clearly seen from this figure that surfactants have a significant effect on the terminal velocity of the droplet though there is no significant effect of surfactant on deformation of the droplet. Similar to what we observed on a nearly-spherical droplet in a denser fluid, viscoelasticity has no significant effect in this regime. The viscoelastic stresses are uniform and lower in this regime which makes their effects on the motion and deformation of the droplet negligible.

3.2.2 Dimpled-ellipsoidal cap droplet falling in a less dense fluid

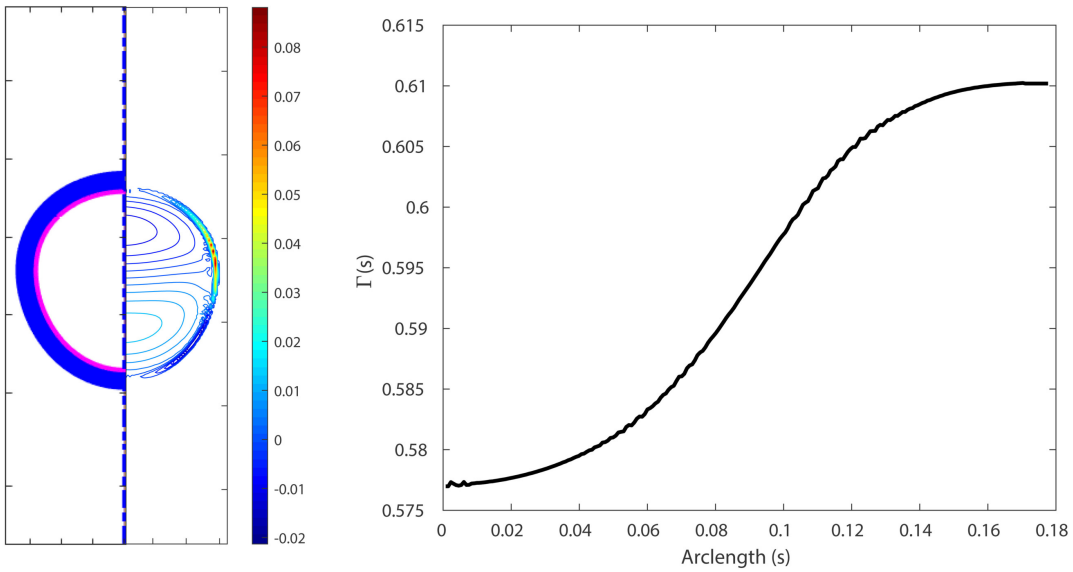

Figure 3.23: A nearly spherical droplet falling in a less dense fluid. (a) The surfactant distribution and constant contours of $trace(\mathbf{B})$ plotted on and inside the droplet. (b) The interfacial surfactant concentration as a function of arclength ($\rho_i/\rho_o = 2, Eo = 1, Mo = 0.01, \beta = 0.5, \alpha = 0.77, Wi = 50, Grid : 64 \times 640$).

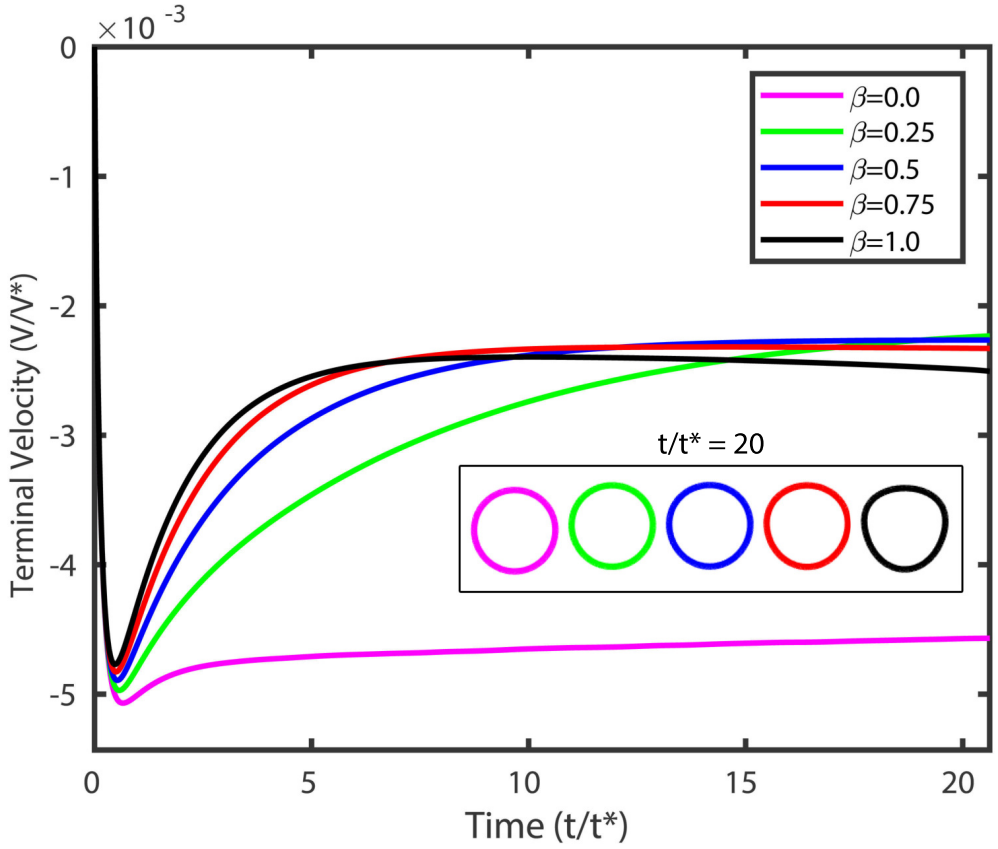

Figure 3.24: Terminal velocity versus non-dimensional time and shape of a nearly spherical droplet droplet (at time $t/t^* = 20$) for different values of elasticity number falling in a less dense fluid ($\rho_i/\rho_o = 2, Eo = 1, Mo = 0.01, \alpha = 0.77, Wi = 50, Grid$: 64×640).

In this regime, a dimpled-ellipsoidal cap droplet falls in a Newtonian fluid due to the gravity forces. Computations are performed by keeping the non-dimensional numbers constant at $\rho_i/\rho_o = 2$, $Pe_s = 10000$, $Pe_c = 100000$, $Da = 32$, $Bi = 0.02$, $\beta = 0.77$, $Wi = 50$ and $\alpha = 0.77$. The *Eötvös* number and Morton number have values $Eo = 50$ and $Mo = 1250$ respectively, where the clean droplet has a dimple at the trailing edge. First, we investigate the effect of surfactant on the terminal velocity and shape of a viscoelastic droplet rising in a tube. For this purpose, computations are performed for different values of elasticity number while keeping the other parameters constant.

First, the effects of surfactants are studied on a dimpled-ellipsoidal cap droplet which is falling in a less dense fluid. When surfactant is added to the system, there is no significant effect on the terminal velocity of the droplet, although there is a minor reduction of terminal velocity because of the Marangoni stresses. Figure 3.26 plots terminal velocity versus non-dimensional time and also the shape of the droplet at the steady state. It's clearly seen from this figure that despite the negligible effect of surfactant on the terminal velocity, surfactants still play an important role in the deformation of the droplet. The aggregated surfactants at the trailing edge of the droplet, which is shown in Fig. 3.25, reduce the surface tension and the weakened surface tension forces then have less ability in balancing other forces, including viscoelastic stresses. The dimple penetrates more into the droplet as a result of reduced surface tension.

The effects of viscoelasticity are then studied using Weissenberg number and solvent viscosity ratio. First, Weissenberg number is changed in the range of $Wi = 0$ to $Wi = 100$ while other values are kept constant. Figure 3.27 shows the terminal velocity versus non-dimensional time for different values of Wi. It shows that in this case, Weissenberg number has no significant effect on the dynamics of the droplet.

Then the effects of solvent viscosity ratio are studied on the motion and deformation of the droplet. Figure 3.28 plots terminal velocity versus non-dimensional time for different values of solvent viscosity ratio. It's worth mentioning that increasing the polymeric viscosity decreases the solvent viscosity ratio and as α decreases, terminal velocity also decreases because of the induced viscoelastic stresses.

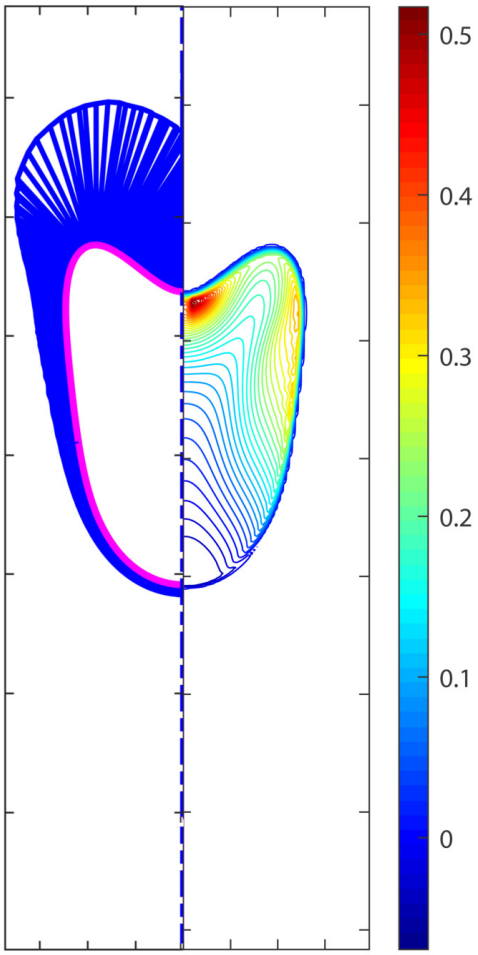

Figure 3.25: A dimpled-ellipsoidal cap droplet falling in a less dense fluid. The surfactant distribution on the droplet interface on left and constant contours of $trace(\mathbf{B})$ on right, are plotted on and inside the droplet ($\rho_i/\rho_o = 2, Eo = 50, Mo = 1250, \beta = 0.5, \alpha = 0.77, Wi = 50, Grid : 64 \times 640$).

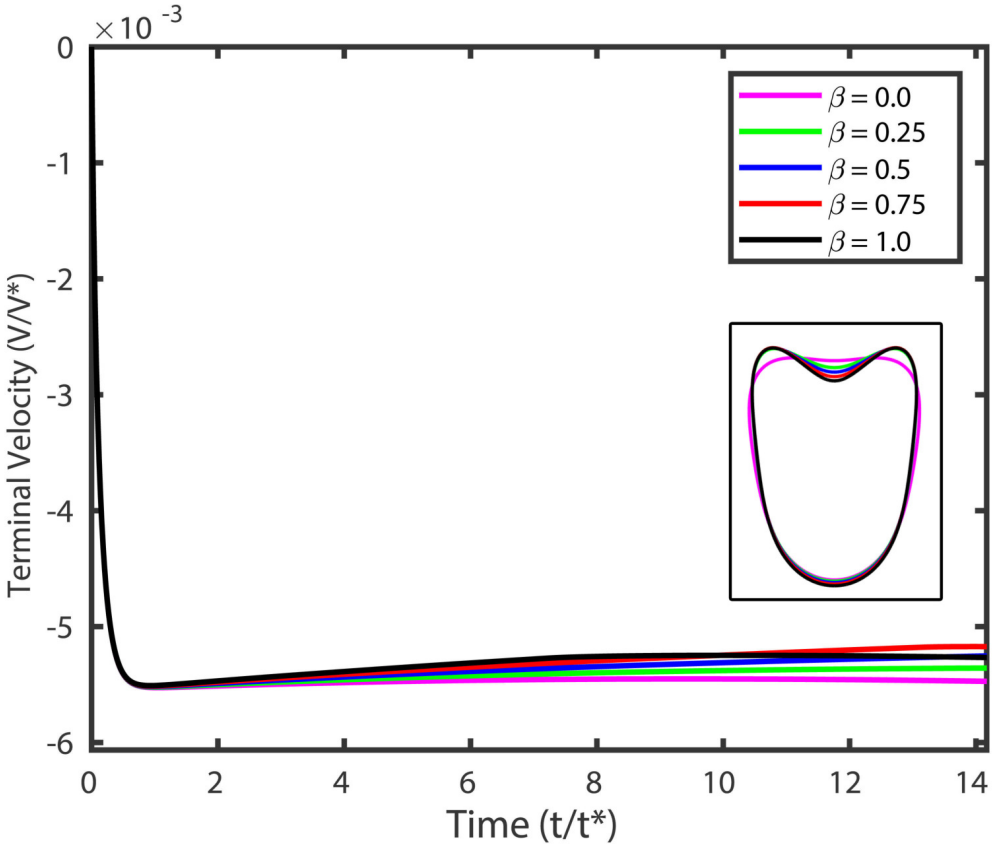

Figure 3.26: Terminal velocity versus non-dimensional time and shape of droplet (at time $t/t^* = 12$) for different values of elasticity number for a viscoelastic dimpled-ellipsoidal cap droplet falling in a less dense fluid ($\rho_i/\rho_o = 2, Eo = 50, Mo = 1250, \alpha = 0.77, Wi = 50, Grid : 64 \times 640$).

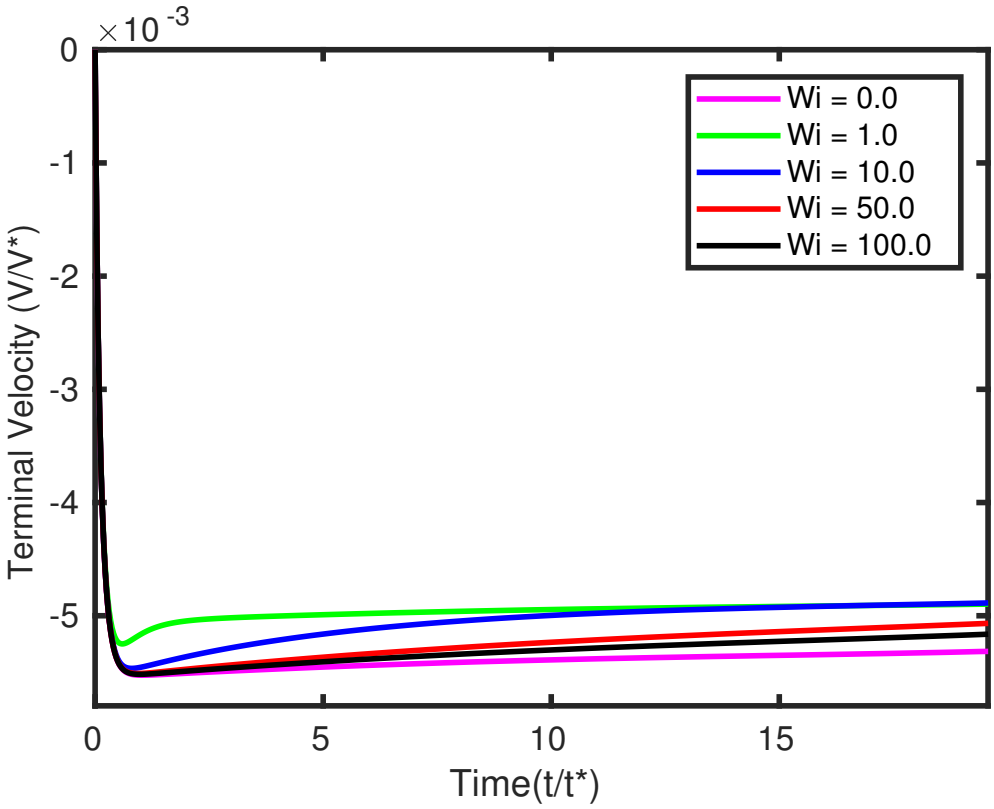

Figure 3.27: Terminal velocity versus non-dimensional time for different values of Weissenberg number for a droplet falling in a less dense fluid ($\rho_i/\rho_o = 2, Eo = 50, Mo = 1250, \alpha = 0.77, \beta = 0.5, Grid : 64 \times 640$).

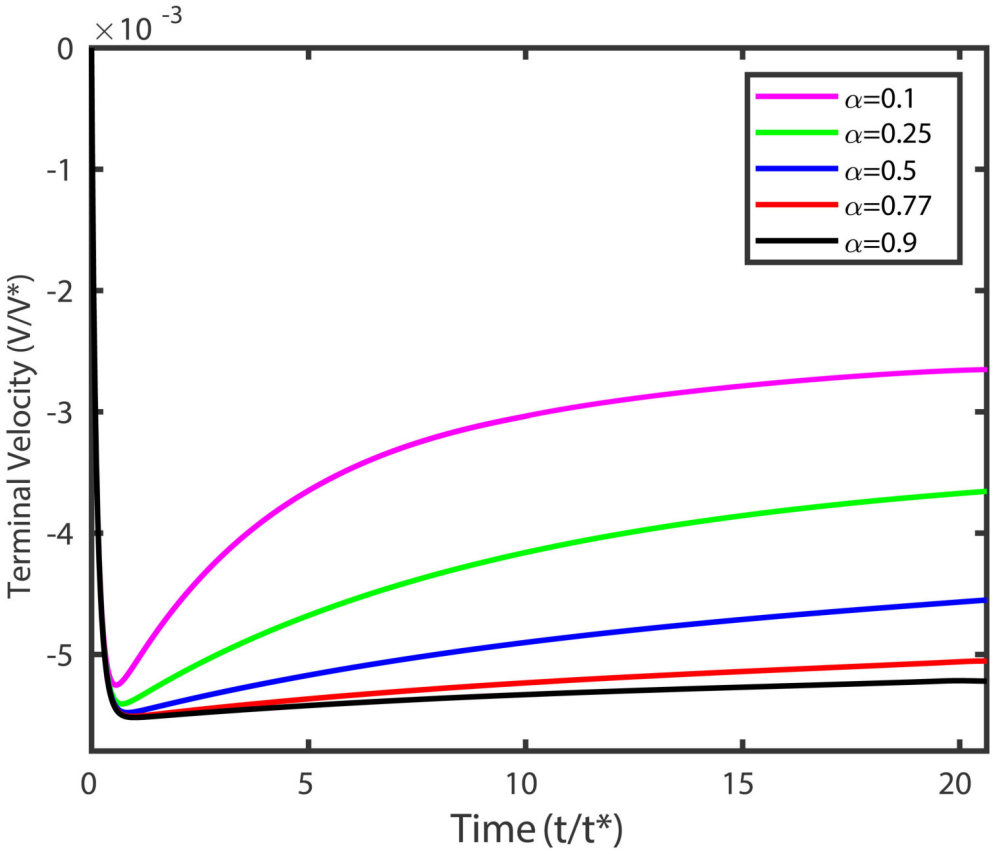

Figure 3.28: Terminal velocity versus non-dimensional time for different values of solvent viscosity ratio for a droplet falling in a less dense fluid ($\rho_i/\rho_o = 2, Eo = 50, Mo = 1250, \beta = 0.5, Wi = 50, Grid : 64 \times 640$).

3.2.3 Skirted droplet falling in a less dense fluid

In this section, a skirted droplet falls in a Newtonian fluid due to the gravity forces. Computations are performed by keeping the non-dimensional numbers constant at $\rho_i/\rho_o = 2$, $Pe_s = 10000$, $Pe_c = 100000$, $Da = 32$, $Bi = 0.02$, $\beta = 0.5$, $Wi = 50$ and $\alpha = 0.77$. The *Eötvös* number and Morton number have values $Eo = 20$ and $Mo = 0.01$ respectively, where a clean droplet becomes skirted at the steady state. Figure 3.29 shows the shape evolution of the droplet as it falls in the ambient fluid. A contaminated/viscoelastic droplet eventually becomes more like a dimpled droplet and also breaks up.

First, we investigate the effect of surfactant on the terminal velocity and shape of a viscoelastic droplet rising in a tube. For this purpose, computations are performed for different values of β while keeping the other parameters constant.

Extensive computations are then performed to investigate the effects of viscoelasticity on the dynamics of the droplet in this regime. For, this purpose, the effects of solvent viscosity ratio are studied on this droplet.

Figure 3.32 plots the viscoelastic stresses as the constant contours of $trace(\mathbf{B})$ for different values of solvent viscosity ratio (α). It's clearly seen that the viscoelastic stresses increase as the solvent viscosity ratio increases. The droplet also gets more deformable as the solvent viscosity ratio increases because the viscoelastic stresses increase specially at the trailing edge of the droplet, and other forces can not balance these extra stresses which in turn lead to more deformation of the droplet.

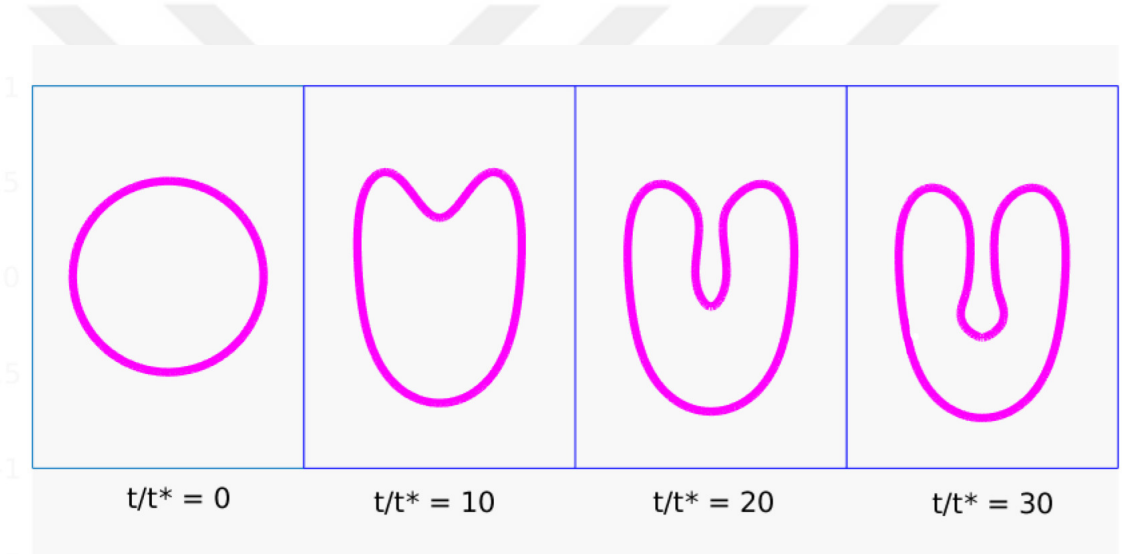

Figure 3.29: Shape evolution of a skirted droplet falling in a less dense fluid ($\rho_i/\rho_o = 2, Eo = 20, Mo = 0.01, \beta = 0.5, Wi = 50, \alpha = 0.77, Grid : 64640$).

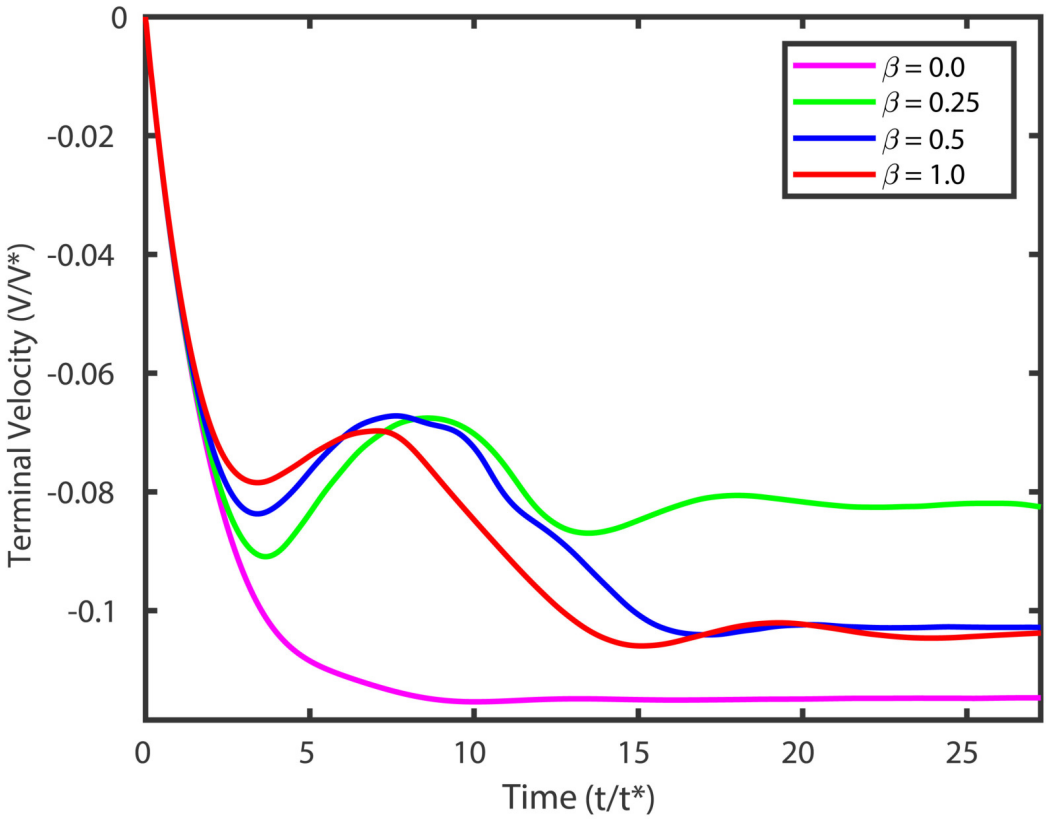

Figure 3.30: Terminal velocity versus non-dimensional time for different values of elasticity number for a skirted droplet falling in a less dense fluid ($\rho_i/\rho_o = 2, Eo = 20, Mo = 0.01, \alpha = 0.77, Wi = 50, Grid : 64 \times 640$).

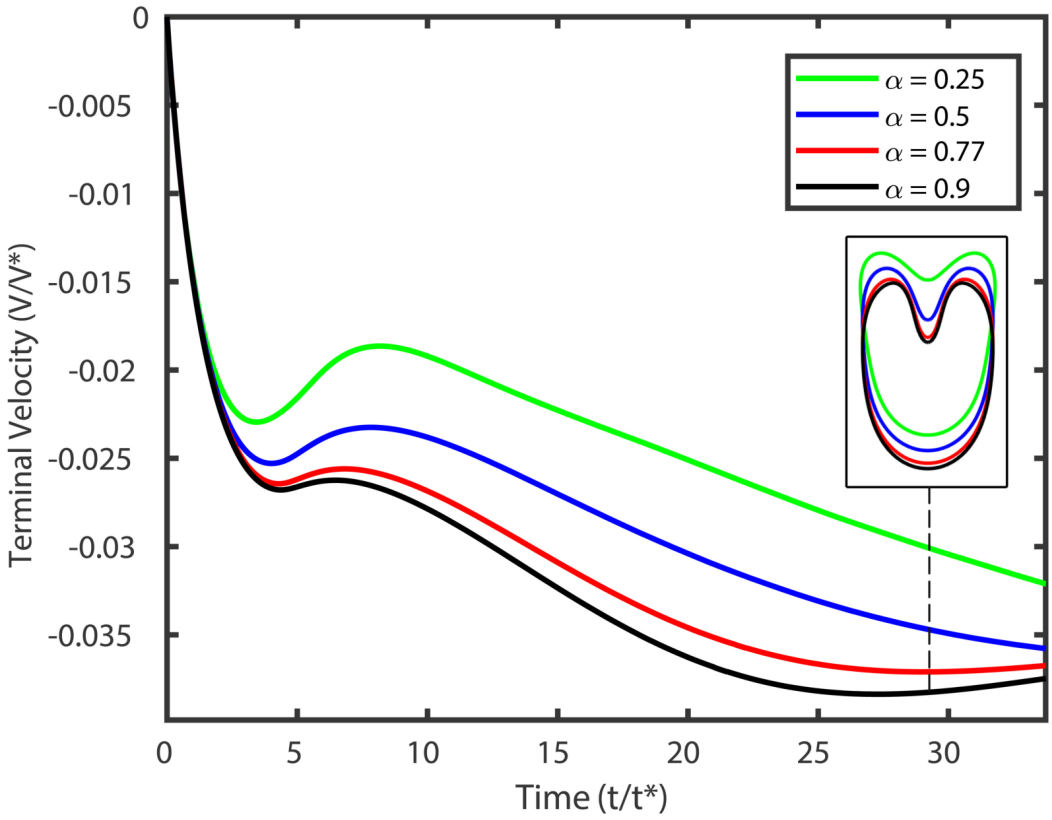

Figure 3.31: Terminal velocity versus non-dimensional time and droplet shape for different values of solvent viscosity ratio for a skirted droplet falling in a less dense fluid ($\rho_i/\rho_o = 2, Eo = 20, Mo = 0.01, \beta = 0.5, Wi = 50, Grid : 64 \times 640$).

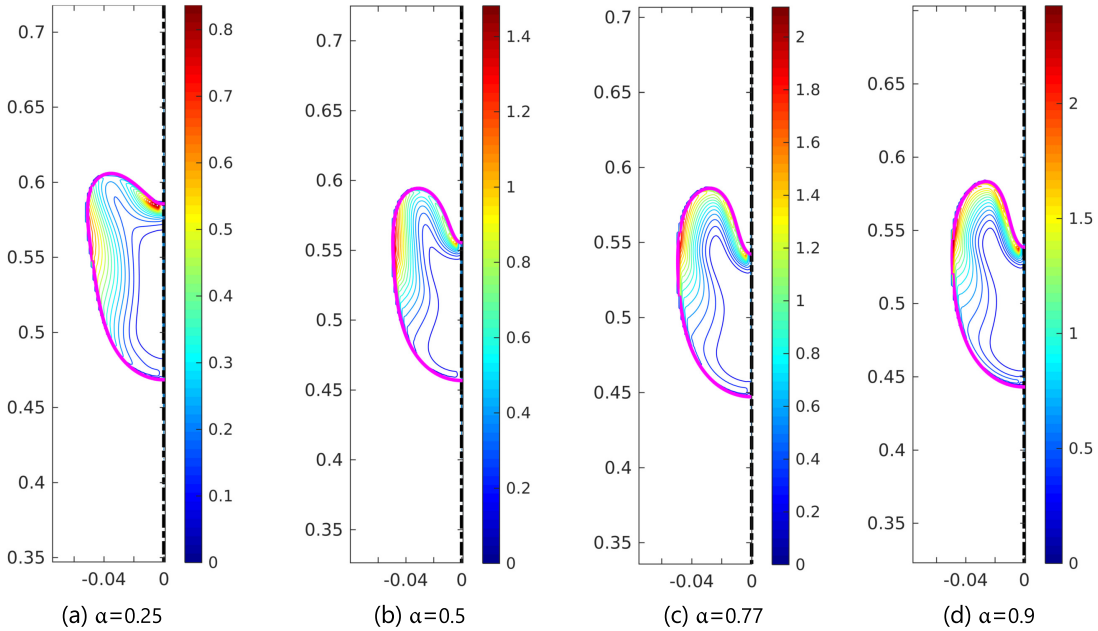

Figure 3.32: Constant contours of $trace(\mathbf{B})$ for a skirted droplet falling in a less dense fluid ($\rho_i/\rho_o = 2, Eo = 20, Mo = 0.01, \beta = 0.5, \alpha = 0.77, Wi = 50, Grid : 64 \times 640$).

Chapter 4

CONCLUSION

A finite-difference/front-tracking method is used to simulate a viscoelastic droplet moving in a contaminated ambient fluid. FENE-CR is used to model viscoelasticity and a non-linear equation of state is used to relate the surface tension to the interfacial surfactant concentration. First, the combined effects of surfactant and viscoelasticity are studied for a nearly spherical, dimpled-ellipsoidal cap and skirted regimes of a droplet which is immersed in a denser fluid. The same regimes are then examined for a droplet which falls in a less dense fluid.

For a droplet which rises in denser fluid, the level of importance varies for surfactant and viscoelasticity for each regime. In a nearly spherical droplet, a change in the elasticity number can remarkably change the dynamics of the droplet. Surfactant induces Marangoni stresses which eventually reduces terminal velocity significantly. In addition, viscoelasticity has no significant effect for this regime. A dimpled-ellipsoidal cap droplet shows sensitivity to both surfactant and viscoelasticity where the dynamics of the droplet can be manipulated by controlling both the surfactant and viscoelasticity variables. Surfactant and viscoelasticity both reduce the terminal velocity because of the Marangoni stresses and the induced viscoelastic stresses at the trailing end of the droplet, respectively. They also make the droplet more deformable. Finally, a skirted droplet is studied. In this regime, viscoelasticity plays a very important role in the dynamics of the droplet, it reduces the terminal velocity considerably and also leads to more deformation of the droplet. In addition, surfactant has negligible effect on the terminal velocity of a skirted droplet, but it can drastically change the deformability of the droplet because of the reduction of surface tension forces especially at the trailing end. Surfactants are surprisingly important in this regime because they change the deformation of the droplet and can lead to break up in severe case. Therefore, the terminal velocity gets oscillatory for some cases of this regime.

Then, the same regimes of a droplet which falls in a less dense fluid are investigated. Sim-

ilar effects are observed for nearly spherical and dimpled-ellipsoidal cap regimes. Although for a skirted droplet falling in a less dense fluid, both the surfactants and viscoelasticity have considerable effects on the dynamics of the droplet which is mostly because of the regime we have picked. In this regime, the droplet is on the verge of dimpled-ellipsoidal cap shape and skirted shape whereas adding surfactants or viscoelasticity to the system changes the steady shape of the skirted droplet to a dimpled-ellipsoidal cap droplet which breaks up in some severe cases. In all the cases of this work, surfactant is studied through the change of elasticity number. Surfactant changes the surface tension of the droplet which can affect the deformation of the droplet. The effect of surfactant on the terminal velocity of the droplet might not be significant for the high *Eötvös* numbers but its effect on the deformability of the droplet might be still considerable. Furthermore, The effects of viscoelasticity are observed using the Weissenberg number and the solvent viscosity ratio. The results of all the regimes show that the solvent viscosity ratio is always of higher importance and smaller changes in the solvent viscosity ratio can lead to more considerable changes in the dynamics of the droplet. Therefore, the solvent viscosity ratio is the best variable to change in order to manipulate the behavior of the droplet.

Generally, surfactants and viscoelasticity reinforce each other's effects on the motion and deformation of a droplet, i.e. both reduce the terminal velocity of the droplet, although their degree of importance depends on the regime. Also, both increase the deformability of the droplet. Surfactants aggregate at the trailing edge of the droplet and reduce surface tension and viscoelasticity induces extra stresses that are pronounced at the trailing edge. Therefore, deformation increases in either case.

4.1 Future work

We can cover more cases such as the study of Newtonian droplet immersed in a viscoelastic fluid where we can observe more interesting phenomenons, the study of the effects of surfactant on the elongation of a Newtonian droplet in a viscoelastic bulk fluid is a good example. The study of the effects of the surfactants and viscoelasticity on a 3D bubbly flow can be also done to tackle more practical problems.

Chapter 5

APPENDIX

5.1 Validation

Grid Convergence of the code is observed and can be seen in Fig. 5.1. Figure 5.1 demonstrates how the difference of terminal velocity for subsequent grid sizes decrease while mesh gets finer which is a result of grid convergence. Observing the relationship between the normalized terminal velocity with the square of non-dimensional grid size $(\Delta x/R)^2$ for different non-dimensional times in Fig. 5.2 also indicates the expected second-order accuracy of the method.

5.2 Validation of an all Newtonian two phase system

First, we observed a clean case ($\beta = 0$) and also a contaminated case ($\beta = 0$) in which both the droplet and bulk fluids are Newtonian. As the droplet moves in a bounded domain, it's possible to validate the results by presenting a relationship between U_T, $U_{T\infty}$ and λ_s, where U_T represents the terminal velocity we get from our calculations, $U_{T\infty}$ is the terminal velocity in the unbounded domain defined in Eq. 3.2 and λ_s is the ratio of the droplet diameter to the diameter of the domain. Figure. 5.3 demonstrates the validation of a contaminated droplet. The terminal velocity of an unconfined sphere from Clift et al. [Clift et al., 2005] is used for the validation of a clean droplet. The correlation is written as:

$$\frac{U_T}{U_{T\infty}} = (1 - {\lambda_s}^2)^{\frac{3}{2}}. \tag{5.1}$$

According to Eq. 5.1 and our results, there is around 6 percent of error which shows our results are in good agreement with the correlation. The terminal velocity of a confined sphere from Clift et al. [Clift et al., 2005] is then used for the validation of a contaminated

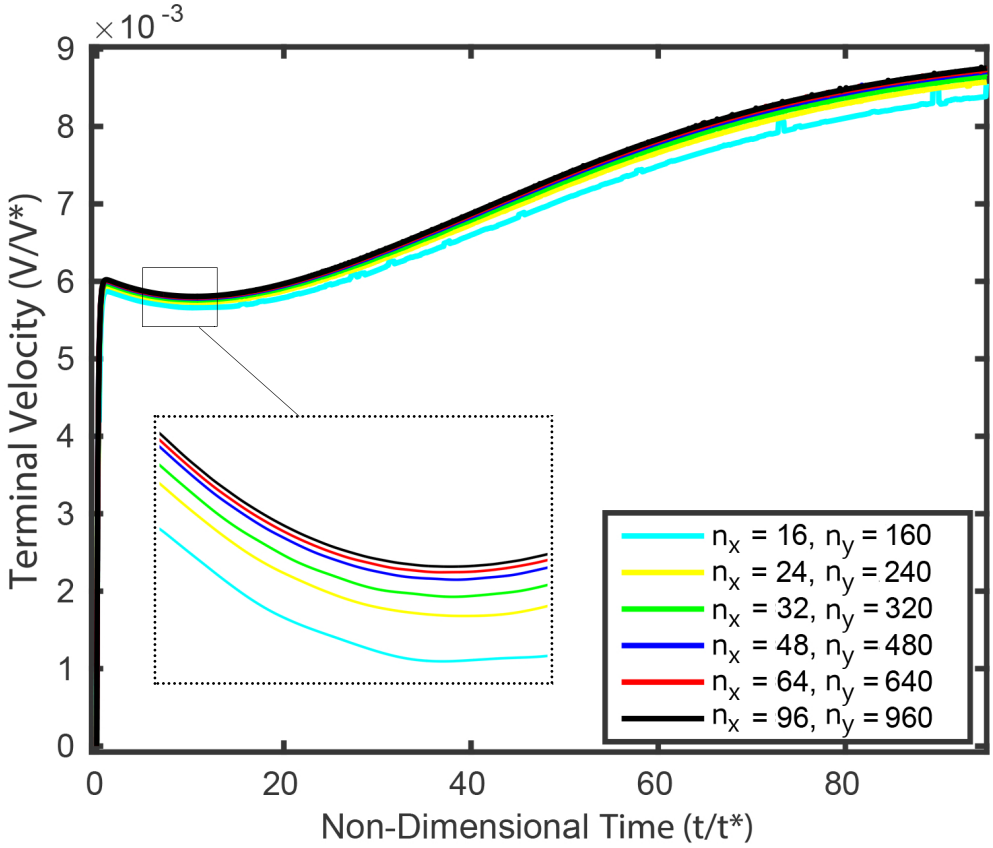

Figure 5.1: Grid Convergence for a contaminated VN case. Terminal velocity versus non-dimensional time for different grid sizes ($\rho_i/\rho_o = 0.5, Eo = 50, Mo = 1250, \alpha = 0.77, Wi = 50, \beta = 0.5, Grid : 64 \times 640$).

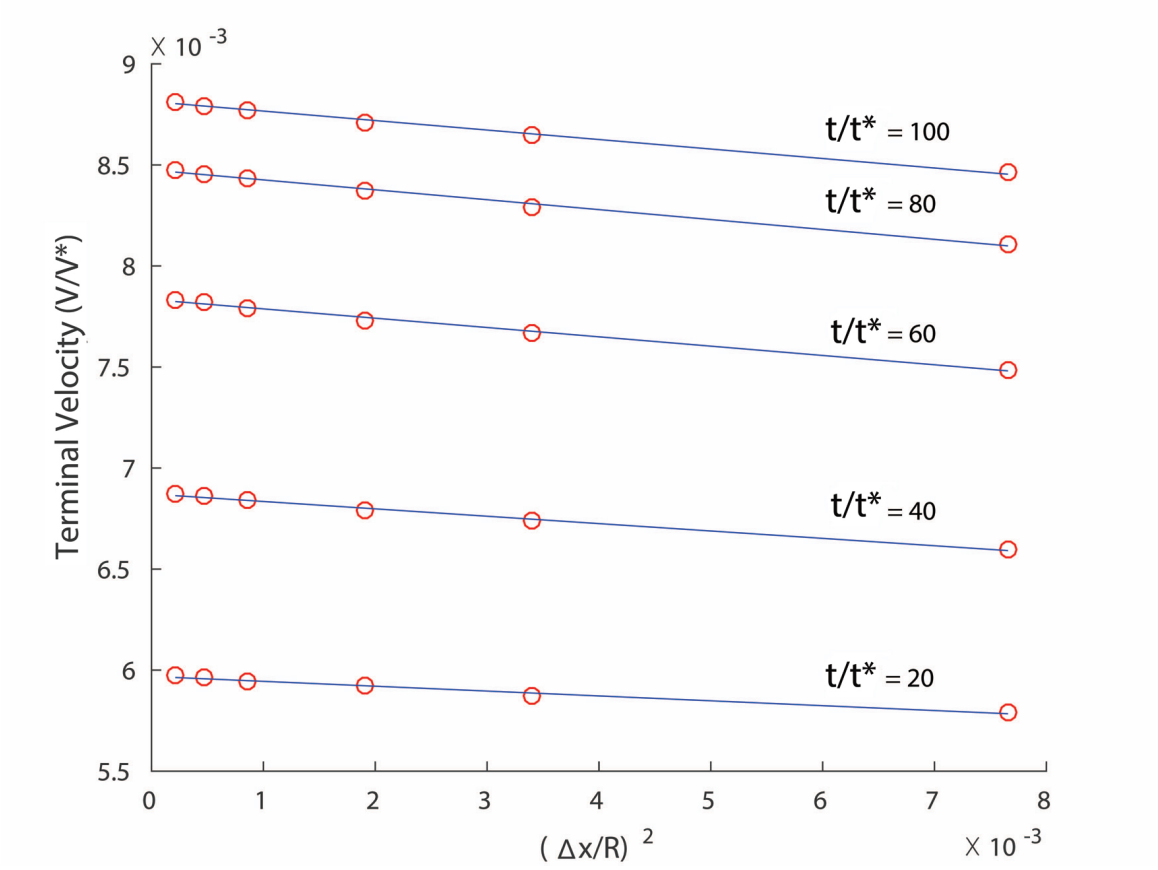

Figure 5.2: Variation of normalized terminal velocity with the square of the non-dimensional grid size ($\rho_i/\rho_o = 0.5, Eo = 50, Mo = 1250, \alpha = 0.77, Wi = 50, \beta = 0.5, Grid : 64 \times 640$).

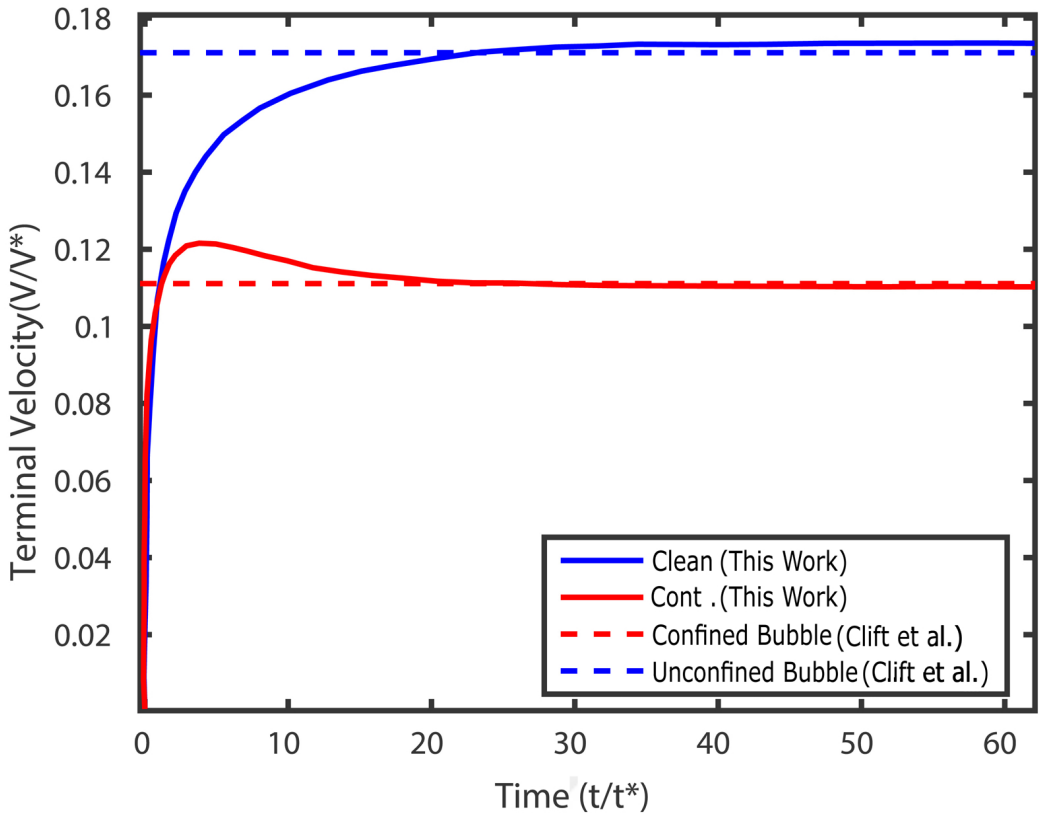

Figure 5.3: Terminal Velocity versus non-dimensional time for a clean $\beta = 0$ and contaminated $\beta = 0$ droplet compared to Clift et el. [Clift et al., 2005] correlation $(\rho_i/\rho_o = 0.5, Eo = 50, Mo = 1250, \alpha = 0.77, Wi = 50, \beta = 0.5, Grid : 64 \times 640)$.

droplet. The correlation is written as:

$$\frac{U_T}{U_{T\infty}} = (1 - 2.2104\lambda_s) + 2.09{\lambda_s}^3 - 0.95{\lambda_s}^{5-1}, \tag{5.2}$$

from which we get $U_T = 0.1170$ and from our calculation we get $U_T = 0.1111$ which represents about 5 percent of error. it's clearly seen from our calculations which are shown in Fig. 5.3 that our results are in good comparison with the correlations of Clift et al. [Clift et al., 2005].

5.3 Validation of a clean viscoelastic droplet in a Newtonian fluid

A viscoelastic test case from You et al. [You et al., 2008] is then used for the validation of a viscoelastic droplet rising in a Newtonian fluid, there is no contamination in this case

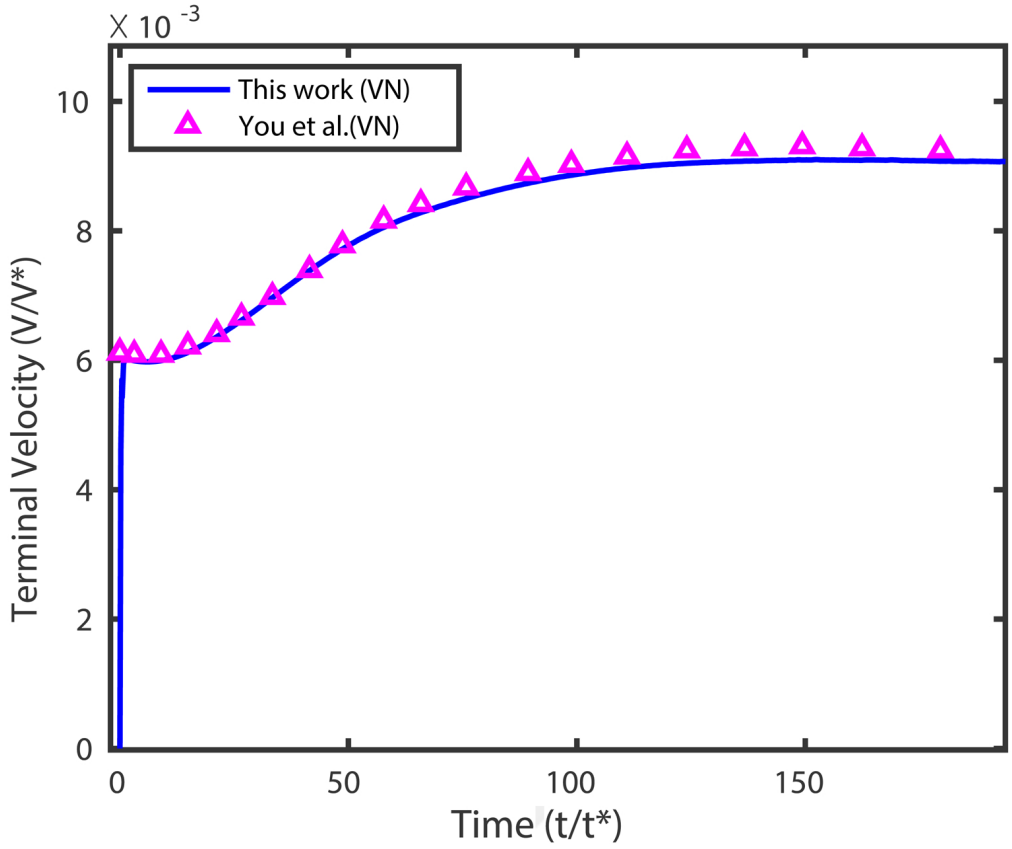

Figure 5.4: Terminal Velocity versus non-dimensional time for a clean viscoelastic droplet in Newtonian fluid ($\rho_i/\rho_o = 0.5, Eo = 50, Mo = 1250, \alpha = 0.77, Wi = 50, \beta = 0.0, Grid : 64 \times 640$).

$\beta = 0$. According to Fig. 5.4, our results are in good agreement with the results of You et al. [You et al., 2008].

BIBLIOGRAPHY

[Almatroushi and Borhan, 2004] Almatroushi, E. and Borhan, A. (2004). Surfactant effect on the buoyancy-driven motion of bubbles and drops in a tube. *Annals of the New York Academy of Sciences*, 1027(1):330–341.

[Bel Fdhila and Duineveld, 1996] Bel Fdhila, R. and Duineveld, P. (1996). The effect of surfactant on the rise of a spherical bubble at high reynolds and peclet numbers. *Physics of Fluids*, 8(2):310–321.

[Beris and Housiadas, 2010] Beris, A. N. and Housiadas, K. D. (2010). Computational viscoelastic fluid mechanics and numerical studies of turbulent flows of dilute polymer solutions. *Modeling and Simulation in Polymers*, pages 1–36.

[Bertola, 2009] Bertola, V. (2009). An experimental study of bouncing leidenfrost drops: comparison between newtonian and viscoelastic liquids. *International journal of heat and mass transfer*, 52(7-8):1786–1793.

[Bertola, 2013] Bertola, V. (2013). Dynamic wetting of dilute polymer solutions: the case of impacting droplets. *Advances in colloid and interface science*, 193:1–11.

[Bertola and Wang, 2015] Bertola, V. and Wang, M. (2015). Dynamic contact angle of dilute polymer solution drops impacting on a hydrophobic surface. *Colloids and Surfaces A: Physicochemical and Engineering Aspects*, 481:600–608.

[Borges et al., 2008] Borges, R., Carmona, M., Costa, B., and Don, W. S. (2008). An improved weighted essentially non-oscillatory scheme for hyperbolic conservation laws. *Journal of Computational Physics*, 227(6):3191–3211.

[Borhan and Pallinti, 1995] Borhan, A. and Pallinti, J. (1995). Buoyancy-driven motion of viscous drops through cylindrical capillaries at small reynolds numbers. *Industrial & engineering chemistry research*, 34(8):2750–2761.

[Borhan and Pallinti, 1999] Borhan, A. and Pallinti, J. (1999). Breakup of drops and bubbles translating through cylindrical capillaries. *Physics of Fluids*, 11(10):2846–2855.

[Chen et al., 2013] Chen, X., Marschall, H., Schäfer, M., and Bothe, D. (2013). A comparison of stabilisation approaches for finite-volume simulation of viscoelastic fluid flow. *International Journal of Computational Fluid Dynamics*, 27(6-7):229–250.

[Chilcott and Rallison, 1988] Chilcott, M. and Rallison, J. M. (1988). Creeping flow of dilute polymer solutions past cylinders and spheres. *Journal of Non-Newtonian Fluid Mechanics*, 29:381–432.

[Clift et al., 2005] Clift, R., Grace, J. R., and Weber, M. E. (2005). *Bubbles, drops, and particles*. Courier Corporation.

[Coates et al., 1992] Coates, P. J., Armstrong, R. C., and Brown, R. A. (1992). Calculation of steady-state viscoelastic flow through axisymmetric contractions with the eeme formulation. *Journal of Non-Newtonian Fluid Mechanics*, 42(1-2):141–188.

[Cuenot et al., 1997] Cuenot, B., Magnaudet, J., and Spennato, B. (1997). The effects of slightly soluble surfactants on the flow around a spherical bubble. *Journal of Fluid Mechanics*, 339:25–53.

[Eggleton and Stebe, 1998] Eggleton, C. D. and Stebe, K. J. (1998). An adsorption–desorption-controlled surfactant on a deforming droplet. *Journal of colloid and interface science*, 208(1):68–80.

[Fattal and Kupferman, 2005] Fattal, R. and Kupferman, R. (2005). Time-dependent simulation of viscoelastic flows at high weissenberg number using the log-conformation representation. *Journal of Non-Newtonian Fluid Mechanics*, 126(1):23–37.

[Frumkin, 1947] Frumkin, A. (1947). On surfactants and interfacial motion. *Zh. Fiz. Khim.*, 21:1183–1204.

[Garner and Nissan, 1946] Garner, F. and Nissan, A. H. (1946). Rheological properties of high-viscosity solutions of long molecules. *Nature*, 158(4018):634.

[Groisman and Steinberg, 2000] Groisman, A. and Steinberg, V. (2000). Elastic turbulence in a polymer solution flow. *Nature*, 405(6782):53.

[Grotberg, 2001] Grotberg, J. B. (2001). Respiratory fluid mechanics and transport processes. *Annual review of biomedical engineering*, 3(1):421–457.

[Grotberg, 2011] Grotberg, J. B. (2011). Respiratory fluid mechanics. *Physics of Fluids*, 23(2):021301.

[Hassager, 1979] Hassager, O. (1979). Negative wake behind bubbles in non-newtonian liquids. *Nature*, 279(5712):402.

[He et al., 1991a] He, Z., Dagan, Z., and Maldarelli, C. (1991a). The influence of surfactant adsorption on the motion of a fluid sphere in a tube. part 1. uniform retardation controlled by sorption kinetics. *Journal of Fluid Mechanics*, 222:132.

[He et al., 1991b] He, Z., Dagan, Z., and Maldarelli, C. (1991b). The influence of surfactant adsorption on the motion of a fluid sphere in a tube. part 1. uniform retardation controlled by sorption kinetics. *Journal of fluid mechanics*, 222:1–32.

[Herrera-Velarde et al., 2003] Herrera-Velarde, J. R., Zenit, R., Chehata, D., and Mena, B. (2003). The flow of non-newtonian fluids around bubbles and its connection to the jump discontinuity. *Journal of non-newtonian fluid mechanics*, 111(2-3):199–209.

[Hill, 1972] Hill, C. T. (1972). Nearly viscometric flow of viscoelastic fluids in the disk and cylinder system. ii: Experimental. *Transactions of the Society of Rheology*, 16(2):213–245.

[Hooper et al., 2001] Hooper, R. W., de Almeida, V. F., Macosko, C. W., and Derby, J. J. (2001). Transient polymeric drop extension and retraction in uniaxial extensional flows. *Journal of non-newtonian fluid mechanics*, 98(2-3):141–168.

[Izbassarov and Muradoglu, 2015] Izbassarov, D. and Muradoglu, M. (2015). A front-tracking method for computational modeling of viscoelastic two-phase flow systems. *Journal of Non-Newtonian Fluid Mechanics*, 223:122–140.

[Izbassarov and Muradoglu, 2016] Izbassarov, D. and Muradoglu, M. (2016). Effects of viscoelasticity on drop impact and spreading on a solid surface. *Physical Review Fluids*, 1(2):023302.

[James and Lowengrub, 2004] James, A. J. and Lowengrub, J. (2004). A surfactant-conserving volume-of-fluid method for interfacial flows with insoluble surfactant. *Journal of computational physics*, 201(2):685–722.

[Johnson and Borhan, 1999] Johnson, R. A. and Borhan, A. (1999). Effect of insoluble surfactants on the pressure-driven motion of a drop in a tube in the limit of high surface coverage. *Journal of colloid and interface science*, 218(1):184–200.

[Larson et al., 1981] Larson, R., Davis, H., and Scriven, L. (1981). Displacement of residual nonwetting fluid from porous media. *Chemical Engineering Science*, 36(1):75–85.

[Lee and Pozrikidis, 2006] Lee, J. and Pozrikidis, C. (2006). Effect of surfactants on the deformation of drops and bubbles in navier–stokes flow. *Computers & fluids*, 35(1):43–60.

[Lee et al., 2011] Lee, W., Walker, L. M., and Anna, S. L. (2011). Competition between viscoelasticity and surfactant dynamics in flow focusing microfluidics. *Macromolecular Materials and Engineering*, 296(3-4):203–213.

[Levich, 1992] Levich, V. (1992). Physicochemical hydrodynamics, prentice-hall, englewood cliffs, nj, 1962. *Google Scholar*.

[Liu et al., 1995] Liu, Y., Liao, T., and Joseph, D. (1995). A two-dimensional cusp at the trailing edge of an air bubble rising in a viscoelastic liquid. *Journal of Fluid Mechanics*, 304:321–342.

[Malaga and Rallison, 2007] Malaga, C. and Rallison, J. (2007). A rising bubble in a polymer solution. *Journal of non-newtonian fluid mechanics*, 141(1):59–78.

[Manual, 2004] Manual, I. C. N. H. S. (2004). Respiratory distress syndrome (rds). *UCSF Childrens Hospital at UCSF Medical Center. The Regents of the University of California*, pages 79–84.

[Marchal and Crochet, 1987] Marchal, J. and Crochet, M. (1987). A new mixed finite element for calculating viscoelastic flow. *Journal of Non-Newtonian Fluid Mechanics*, 26(1):77–114.

[Muradoglu and Tryggvason, 2008] Muradoglu, M. and Tryggvason, G. (2008). A front-tracking method for computation of interfacial flows with soluble surfactants. *Journal of computational physics*, 227(4):2238–2262.

[Muradoglu and Tryggvason, 2014] Muradoglu, M. and Tryggvason, G. (2014). Simulations of soluble surfactants in 3d multiphase flow. *Journal of Computational Physics*, 274:737–757.

[Noh et al., 1993] Noh, D., Kang, I., and Leal, L. G. (1993). Numerical solutions for the deformation of a bubble rising in dilute polymeric fluids. *Physics of Fluids A: Fluid Dynamics*, 5(6):1315–1332.

[Nooranidoost et al., 2016] Nooranidoost, M., Izbassarov, D., and Muradoglu, M. (2016). Droplet formation in a flow focusing configuration: Effects of viscoelasticity. *Physics of Fluids*, 28(12):123102.

[Olbricht, 1996] Olbricht, W. (1996). Pore-scale prototypes of multiphase flow in porous media. *Annual review of fluid mechanics*, 28(1):187–213.

[Olgac and Muradoglu, 2013] Olgac, U. and Muradoglu, M. (2013). Computational modeling of unsteady surfactant-laden liquid plug propagation in neonatal airways. *Physics of Fluids*, 25(7):071901.

[Owens and Phillips, 2002] Owens, R. G. and Phillips, T. N. (2002). *Computational rheology*, volume 14. World Scientific.

[Peskin, 1977] Peskin, C. S. (1977). Numerical analysis of blood flow in the heart. *Journal of computational physics*, 25(3):220–252.

[Sarkar and Schowalter, 2000] Sarkar, K. and Schowalter, W. R. (2000). Deformation of a two-dimensional viscoelastic drop at non-zero reynolds number in time-periodic extensional flows. *Journal of non-newtonian fluid mechanics*, 95(2-3):315–342.

[Schenck and Fiegel, 2016] Schenck, D. M. and Fiegel, J. (2016). Tensiometric and phase domain behavior of lung surfactant on mucus-like viscoelastic hydrogels. *ACS applied materials & interfaces*, 8(9):5917–5928.

[Sjoblom, 2005] Sjoblom, J. (2005). *Emulsions and emulsion stability: Surfactant science series/61*. CRC Press.

[Sostarecz and Belmonte, 2003] Sostarecz, M. C. and Belmonte, A. (2003). Motion and shape of a viscoelastic drop falling through a viscous fluid. *Journal of Fluid Mechanics*, 497:235–252.

[Stone, 1990] Stone, H. (1990). A simple derivation of the time-dependent convective-diffusion equation for surfactant transport along a deforming interface. *Physics of Fluids A: Fluid Dynamics*, 2(1):111–112.

[Stone and Leal, 1990] Stone, H. A. and Leal, L. G. (1990). The effects of surfactants on drop deformation and breakup. *Journal of Fluid Mechanics*, 220:161186.

[Sugiyama et al., 2001] Sugiyama, K., Takagi, S., and Matsumoto, Y. (2001). Multi-scale analysis of bubbly flows. *Computer methods in applied Mechanics and Engineering*, 191(6-7):689–704.

[Takagi and Matsumoto, 2011] Takagi, S. and Matsumoto, Y. (2011). Surfactant effects on bubble motion and bubbly flows. *Annual Review of Fluid Mechanics*, 43:615–636.

[Takemura and Yabe, 1999] Takemura, F. and Yabe, A. (1999). Rising speed and dissolution rate of a carbon dioxide bubble in slightly contaminated water. *Journal of Fluid Mechanics*, 378:319–334.

[Tanner, 1970] Tanner, R. (1970). A theory of die-swell. *Journal of Polymer Science Part A-2: Polymer Physics*, 8(12):2067–2078.

[Tasoglu et al., 2008] Tasoglu, S., Demirci, U., and Muradoglu, M. (2008). The effect of soluble surfactant on the transient motion of a buoyancy-driven bubble. *Physics of fluids*, 20(4):040805.

[Tasoglu et al., 2010] Tasoglu, S., Kaynak, G., Szeri, A. J., Demirci, U., and Muradoglu, M. (2010). Impact of a compound droplet on a flat surface: A model for single cell epitaxy. *Physics of Fluids*, 22(8):082103.

[Tretheway and Leal, 1999] Tretheway, D. C. and Leal, L. G. (1999). Surfactant and viscoelastic effects on drop deformation in 2-d extensional flow. *AIChE journal*, 45(5):929–937.

[Tryggvason et al., 2011] Tryggvason, G. G., Scardovelli, R., and phane Zaleski, S. (2011). *Direct Numerical Simulations of Gas-Liquid Multiphase Flows*. Cambridge University Press.

[Unverdi and Tryggvason, 1992] Unverdi, S. O. and Tryggvason, G. (1992). A front-tracking method for viscous, incompressible, multi-fluid flows. *Journal of computational physics*, 100(1):25–37.

[Wissler, 1963] Wissler, E. H. (1963). Physicochemical hydrodynamics (levich, veniamin g.).

[You et al., 2008] You, R., Borhan, A., and Haj-Hariri, H. (2008). A finite volume formulation for simulating drop motion in a viscoelastic two-phase system. *Journal of Non-Newtonian Fluid Mechanics*, 153(2):109–129.

[Zhang and Finch, 2001] Zhang, Y. and Finch, J. (2001). A note on single bubble motion in surfactant solutions. *Journal of fluid Mechanics*, 429:63–66.